AERODYNAMICS OF WRAPAROUND FINS IN SUPERSONIC FLOW

Brett Landon Wilks

**System Simulation and Development Directorate
Aviation and Missile Research, Development, and
Engineering Center**

April 2006

AMRDEC
STRENGTH THROUGH TECHNOLOGY

DESTRUCTION NOTICE

DISCLAIMER

TRADE NAMES

REPORT DOCUMENTATION PAGE			Form Approved OMB No. 074-0188
Public reporting burden for this collection of information is estimated to average 1 hour per response, including the time for reviewing instructions, searching existing data sources, gathering and maintaining the data needed, and completing and reviewing this collection of information. Send comments regarding this burden estimate or any other aspect of this collection of information, including suggestions for reducing this burden to Washington Headquarters Services, Directorate for Information Operations and Reports, 1215 Jefferson Davis Highway, Suite 1204, Arlington, VA 22202-4302, and to the Office of Management and Budget, Paperwork Reduction Project (0704-0188), Washington, DC 20503			

1. AGENCY USE ONLY	2. REPORT DATE April 2006	3. REPORT TYPE AND DATES COVERED Final	

4. TITLE AND SUBTITLE Aerodynamics of Wraparound Fins in Supersonic Flow	5. FUNDING NUMBERS
6. AUTHOR(S) Brett Landon Wilks	

7. PERFORMING ORGANIZATION NAME(S) AND ADDRESS(ES) Commander, U.S. Army Research, Development, and Engineering Command ATTN: AMSRD-AMR-SS-AT Redstone Arsenal, AL 35898	8. PERFORMING ORGANIZATION REPORT NUMBER TR-AMR-SS-06-15

9. SPONSORING / MONITORING AGENCY NAME(S) AND ADDRESS(ES)	10. SPONSORING / MONITORING AGENCY REPORT NUMBER

11. SUPPLEMENTARY NOTES

12a. DISTRIBUTION / AVAILABILITY STATEMENT Approved for public release; distribution is unlimited.	12b. DISTRIBUTION CODE A

13. ABSTRACT *(Maximum 200 Words)*

Existing supersonic fin theory has been modified to compute the pressure distribution over a Wraparound Fin (WAF). Evvard's theory has been used to calculate the pressure loading due to Angle-of-Attack (AoA) on a WAF by including fin curvature as a variable in the definition of the zones of influence. Evvard's theory uses the intersections of the fin surface and the Mach cones originating from the leading edge discontinuities to split the fin surface into regions of influence. For a planar fin, the intersections are linear; however, the intersections on a curved fin form curved lines. By redefining the Mach lines to account for fin curvature and using an empirically derived induced AoA, the application of Evvard's theory can be extended to accurately compute the unique aerodynamic characteristic of WAFs.

14. SUBJECT TERMS Wraparound, Supersonic, Evvard, Curved	15. NUMBER OF PAGES 62
	16. PRICE CODE

17. SECURITY CLASSIFICATION OF REPORT UNCLASSIFIED	18. SECURITY CLASSIFICATION OF THIS PAGE UNCLASSIFIED	19. SECURITY CLASSIFICATION OF ABSTRACT UNCLASSIFIED	20. LIMITATION OF ABSTRACT SAR

NSN 7540-01-280-5500

Standard Form 298 (Rev. 2-89)
Prescribed by ANSI Std. Z39-18
298-102

TABLE OF CONTENTS

LIST OF ILLUSTRATIONS

LIST OF ILLUSTRATIONS (CONTD)

LIST OF ILLUSTRATIONS (CONCLD)

LIST OF TABLES

I. INTRODUCTION

Wraparound Fins (WAFs) are a family of fins that, when stowed, conform or "wraparound" the surface of a cylindrical body. As a result of the packaging advantage WAFs have over planar fins, WAFs are prevalent on tube-launched missile and rocket systems. Several fielded missiles, rockets and munitions utilize WAFs for stability; among these systems are Multiple Launch Rocket System (MLRS), The Army Combined Arms Weapon System (TACAWS), Advanced Precision Kill Weapon System (APKWS), Line-of-Sight Antitank (LOSAT), Brilliant Anti-Tank (BAT), Compact Kinetic Energy Missile (CKEM), Hydra-70, and variants of the Zuni rocket. Figure 1 shows a set of four WAFs both stowed around the body of a rocket and deployed.
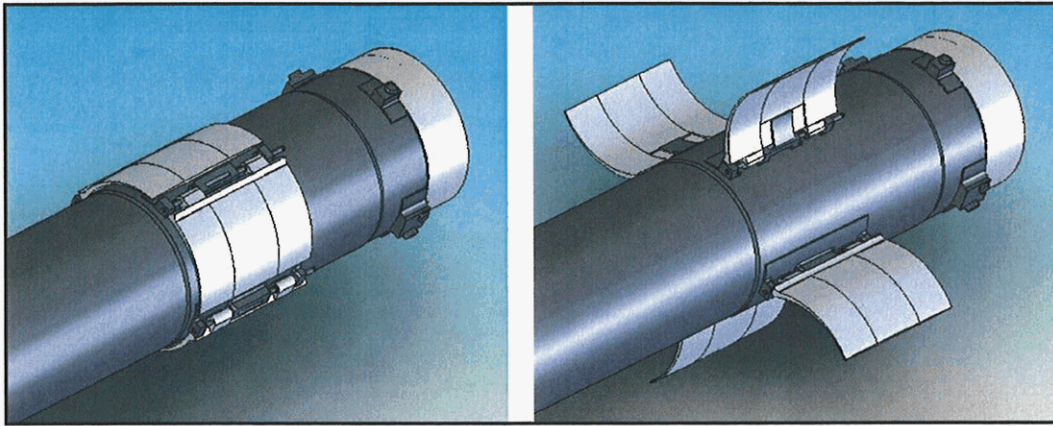
Figure 1. Packaging Advantage of WAFs

The geometry of a WAF is typically determined by the diameter of the missile and the number of fins. The curved span of the WAF is typically the missile circumference divided by the number of fins, and the angle of curvature is 360 degrees divided by the number of fins. A majority of the systems utilizing WAFs have four fins; therefore, a WAF with 90 degrees of curvature is common. However, several 2.75-inch rockets are equipped with three WAFs for stability. BAT employs four overlapping WAFs for stability with a curvature angle of 180 degrees.

WAFs, however, do come with aerodynamic peculiarities. Systems equipped with WAFs exhibit significant rolling moments at zero incidence. The "induced" rolling moment is documented as a function of Mach number and Angle-of-Attack (AoA).

A. Historical Perspectives

1. United States Army

A series of tests were conducted between 1971 and 1976 by the Aeroballistics Directorate of the U.S. Army Missile Research, Development, and Engineering Center (AMRDEC) to identify alternative stabilizing devices [6-10]. Among these devices were WAFs, ringtails, and flares. Limited data were collected on several WAF geometries on a splitter-plate and on a generic 4-inch diameter body with a 2-caliber secant ogive nose and an 8-caliber cylindrical after-body. The fins tested were limited to 90 degrees of curvature.

In terms of stability, the U.S. Army concluded that WAFs perform similarly to planar fins of equivalent projected plan-form shape. It was also noted that WAFs produced a substantial amount of rolling moment which varied with AoA and Mach number. These variations in rolling moment could possibly lead to significant dynamic problems including Magnus instability and roll rate variations during ballistic flight if not compensated for correctly. Furthermore, the rolling moment was found to be a strong function of Mach number as the direction of the rolling moment changed near Mach 1.0. In supersonic flow, the fins produced an induced normal force away from the center of curvature at zero incidence. Conversely, the fins produced an induced normal force toward the center of curvature in subsonic flow at zero incidence.

2. United States Air Force

In the late 1980's, the U.S. Air Force (USAF) began investigating the cause of the low-incidence rolling moment generated by their tube-launched missile systems equipped with WAFs [1,14,18]. The USAF used several techniques to investigate the flow field near a WAF including free-flight gun tests, wind-tunnel tests (with and without the aid of pressure-sensitive paint), and Computational Fluid Dynamics (CFD). The USAF also investigated several methods of reducing the magnitude of the induced roll by slotting WAFs and altering the fin-body junction angle. A majority of the testing was performed on a 2.22 aspect ratio rectangular fin with a thickness-to-chord ratio of 12.5 percent and a 45-degree leading edge wedge angle. Interest was focused between Mach 2.15 and Mach 3.83.

According to the USAF studies, the leading edge of the fin causes a bow shock that interacts with the convex and concave sides of the fin much differently. On the concave side of the fin, the shock is focused near the center of curvature causing a region of relatively high pressure which diminishes as the shock becomes more acute at higher Mach numbers. The convex side of the fin shows a small region of high relative pressure near the body-fin juncture that intensifies as the Mach number increases. The result is a net force away from the center of curvature which decreases with Mach number.

B. Current Perspective

The U.S. Army Aviation and Missile Command tested a series of WAFs on a splitter-plate at the Lockheed Martin Missile and Fire Control High-Speed Wind-Tunnel (LMMFC HSWT) in Dallas, Texas in January of 2005, with the goal of developing a design methodology for WAFs. The test data for the WAF show two notable features. The more notable feature is an induced normal force on the WAF at zero incidence which leads to an induced rolling moment when the fins are used on a missile system. The second difference is a slight increase in the normal force slope with respect to AoA with increasing curvature. Since there is only a slight change in the normal force slope, it appears that the fin curvature effectively generates an induced AoA when compared to a planar fin of the same projected plan-form shape.

II. METHODOLOGY

In order to develop a design methodology for WAFs, the effect of curvature on the pressure loading of a WAF must be understood. The pressure-sensitive paint results, presented in Reference 14, show the pressure loading of a WAF at zero incidence is similar to the pressure loading of a planar fin at an AoA. The pressure loading has distinct divisions that appear much like Mach lines. The interior of the WAF has a fairly constant pressure and the tip of the fin has a much lower pressure. The pressure loading is similar to the results obtained from Evvard's theory for a planar fin at a non-zero incidence. Therefore, it is reasonable to assume that the pressure loading of a WAF can be estimated with Evvard's theory with the addition of an induced AoA. In addition to obtaining the normal force and hinge moment of the fin, the geometry of the WAF can then be used to obtain the side force and root bending moment from the pressure distribution.

A. Induced AoA

At the 2005 LMMFC HSWT, fin-alone data was gathered via a splitter-plate for three different aspect ratio rectangular fins with various curvature. The fins were attached to a six-component balance; therefore, a complete force-and-moment data set was gathered. The zero normal force AoA of each tested fin was derived from the test data, and a correlation dependent on Mach number, aspect ratio, and fin curvature was formulated for the induced AoA. The geometry of the fins tested is tabulated in Table 1, and a photo of the test fins can be seen in Figure 2.

Table 1. Wind-Tunnel Fin Geometries

| Cfg	Root Chord in.	Tip Chord in.	Reference Length in.	Reference Area in.^{2}	Curvature Angle deg.	Curvature Radius in.	Aspect Ratio	Taper Ratio	Exposed Semi-Span in.	LE Sweep Angle deg.	Projected Plan-Form Area in.^{2}	Wetted Plan-Form Area in.^{2}
	cr	ct	L_{ref}	S_{ref}	θ	R	AR	λ	b/2	Λ	S_p	S_w
F010	4.2500	4.2500	4.2500	12.75	0.0	∞	1.4118	1.0	3.000	0.0	12.7500	12.7500
F012	"	"	"	"	45.0	3.9197	1.4118	"	"	0.0	"	13.0837
F014	"	"	"	"	90.0	2.1213	1.4118	"	"	0.0	"	14.1616
F016	"	"	"	"	135.0	1.6236	1.4118	"	"	0.0	"	16.2584
F018	"	"	"	"	180.0	1.5000	1.4118	"	"	0.0	"	20.0277
F020	3.0000	3.0000	3.0000	12.75	0.0	∞	2.8333	1.0	4.250	0.0	12.7500	12.7500
F024	"	"	"	"	90.0	3.0052	2.8333	"	"	0.0	"	14.1617
F026	"	"	"	"	135.0	2.3001	2.8333	"	"	0.0	"	16.2584
F030	4.9100	2.4550	3.6825	12.75	0.0	∞	1.8824	0.5	3.466	35.0	12.7635	12.7635
F034	"	"	"	"	90.0	2.4508	1.8824	"	"	35.0	"	14.1765
F036	"	"	"	"	135.0	1.8758	1.8824	"	"	35.0	"	16.2757
F040	3.6825	3.6825	3.6825	12.75	0.0	∞	1.8824	1.0	3.466	0.0	12.7635	12.7635
F044	"	"	"	"	90.0	2.4508	1.8824	"	"	0.0	"	14.1765
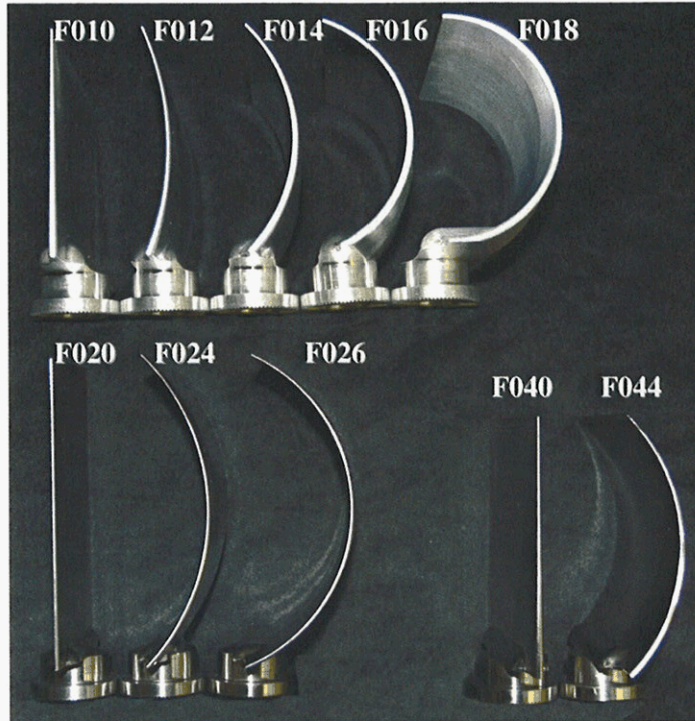
Figure 2. Photo of Tested WAFs

B.   AoA Dependence

In the late 1940's, John Evvard [11,12] and others [13,15,16] solved the potential flow equations for a point-source distribution over a planar fin in supersonic flow. In order to utilize Evvard's solution, the fin is divided into regions of similar disturbance types governed by the Mach lines emanating from leading edge discontinuities. An additional region can form on swept fins when the Mach line originating from the root leading edge discontinuity is reflected by the fin tip (Region V in Fig. 3). Each region consists of one or more of the three fundamental disturbance types: infinite fin, triangular fin, and fin tip. The potential flow solution applicable to each region is used to determine the pressure differential of the upper and lower surface of the fin as a function of AoA.

Since the regions of flow are defined by the intersection of the Mach cones and the fin surface, curvature can have a significant effect on the zoning of the fin surface. While a Mach cone intersects a planar fin with a linear Mach line, the intersection of a Mach cone and a WAF produces a curved Mach line. As the curvature increases, the area of the fin in the region that creates the largest pressure differential, Region I, also increases. The result is an increase in the normal force slope with respect to AoA with curvature. Figure 3 illustrates the effect of curvature on the dividing Mach lines.
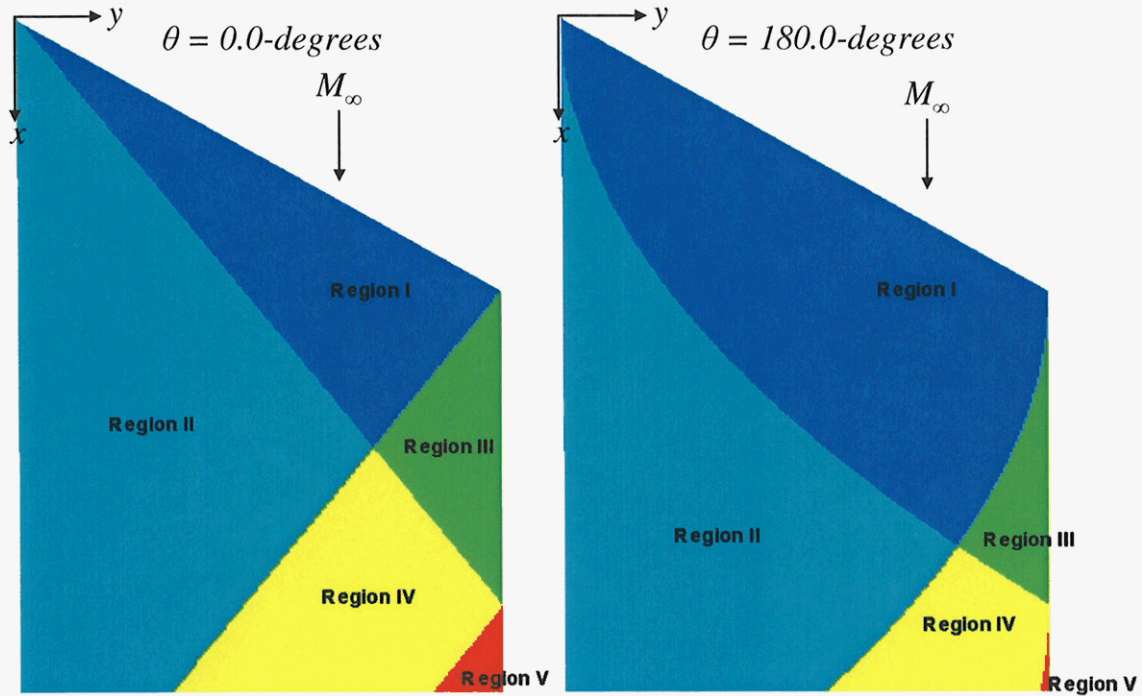
Figure 3. Curvature Effect on Mach Lines at Mach 1.6

III. THEORY

The theoretical modifications required to obtain the pressure loading on a WAF surface begin with geometry. In order to apply Evvard's theory, the fin of interest must be divided into incremental surface panels with a control point in the center of each panel. The curvature angle and projected plan-form fin geometry are used to define an array of 3-Dimensional (3-D) control points and the local surface slopes at each control point. The fin geometry and the flow conditions are then used to define the Mach lines. Once the control points are zoned based on their position relative to the Mach lines, Evvard's theory is used to determine the pressure differential at each control point. Finally, the incremental panel area, the local surface slope, and the differential pressure coefficient are used to determine the normal force, hinge moment, side force, and root bending moment coefficients of the fin.

A. Curved Fin Geometry

Defining the geometry of the WAF surface is the basis of the analysis. The fin is divided into the desired number of span-wise and chord-wise panels, and a control point is positioned in the center of each control panel. With the chord-wise (x) and span-wise (y) coordinates of each control point known, the magnitude of the z-coordinate is determined based on the curvature of the fin. Figure 4 shows the basic nomenclature that will be used to describe the geometry of a WAF.
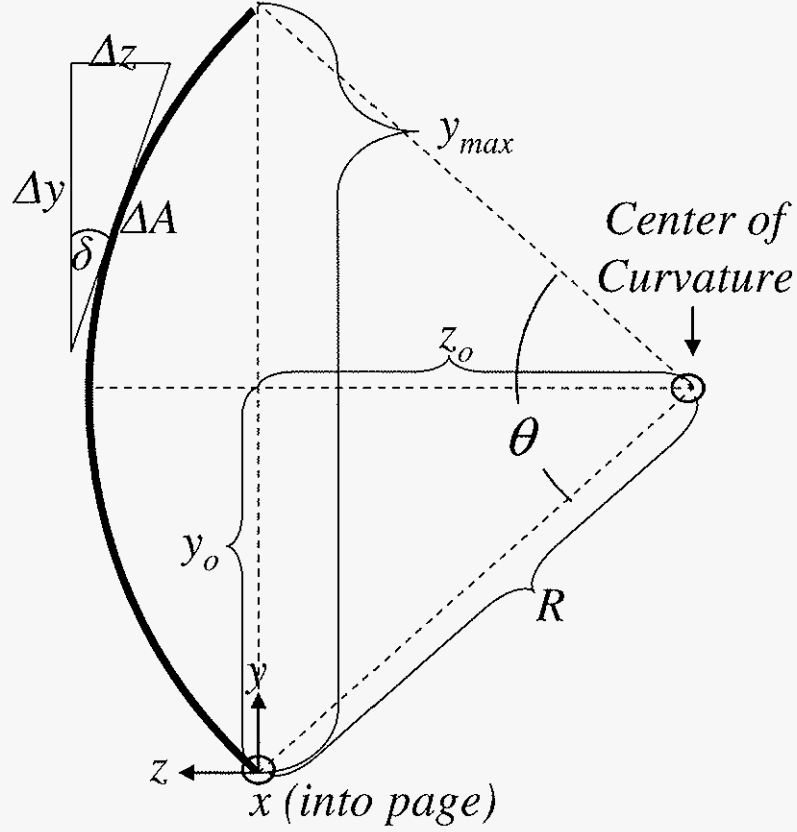
Figure 4: Curved Fin Geometry

The center of curvature of the fin is defined by:

$$y_o = \frac{y_{max}}{2.0} \tag{1}$$

$$R = \frac{y_o}{\sin\left(\frac{\theta}{2.0}\right)} \tag{2}$$

$$z_o = -\sqrt{R^2 - y_o^2} \quad . \tag{3}$$

Once the center of curvature is known, the z-component of the fin surface can be obtained from the equation of a circle with center y_o, z_o.

$$z = \sqrt{R^2 - (y - y_o)^2} + z_o \tag{4}$$

Furthermore, the local surface slope of each control point will be used to obtain the incremental panel area on which the pressure differential acts to produce a force on the fin in the y-direction; i.e. side force. The surface slope angle at each control point is defined as:

$$\delta = \tan^{-1}\left(dz\big/dy\right) = \tan^{-1}\left(\frac{-(y-y_o)}{\sqrt{R^2-(y-y_0)^2}}\right).$$

(5)

B.   Dividing Mach Lines

The dividing Mach lines of a WAF are derived from the intersection of the Mach cone originating at the fin tips and the fin surface. Figure 5 illustrates the intersection of the two surfaces showing the coordinates that are referenced in Equations (6) through (12).
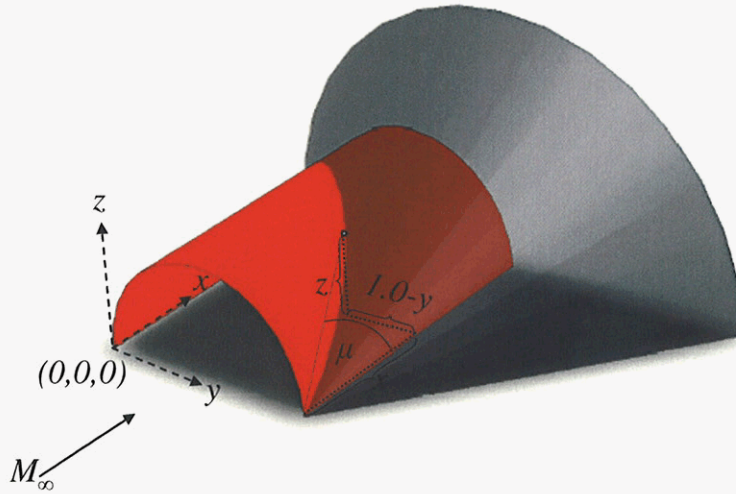

Figure 5. Mach Cone - WAF Surface Intersection

For a planar fin, the intersection of the Mach cone emanating from the fin tip and the surface is simply a line defined by:

$$\tan\mu = \frac{1.0-y}{x}$$

(6)

where,

$$\mu = \sin^{-1}\left(1\big/M\right).$$

(7)

7

As seen from Figure 5, the line describing the intersection of the Mach cone and a WAF surface can be redefined to include the z-component as:

$$\tan \mu = \frac{\sqrt{(1.0 - y)^2 + z^2}}{x} \ .$$

(8)

The Mach cone boundaries and their reflection lines are used to divide the fin into as many as five regions of flow. The regions shown in Figure 6 can be defined as:

Region 1: $x < x_1$ and $x < x_2$

Region 2: $x > x_1$ but $x < x_2$

Region 3: $x > x_2$ but $x < x_1$

Region 4: $x > x_1$ and $x > x_2$ but $x < x_3$

Region 5: $x > x_3$
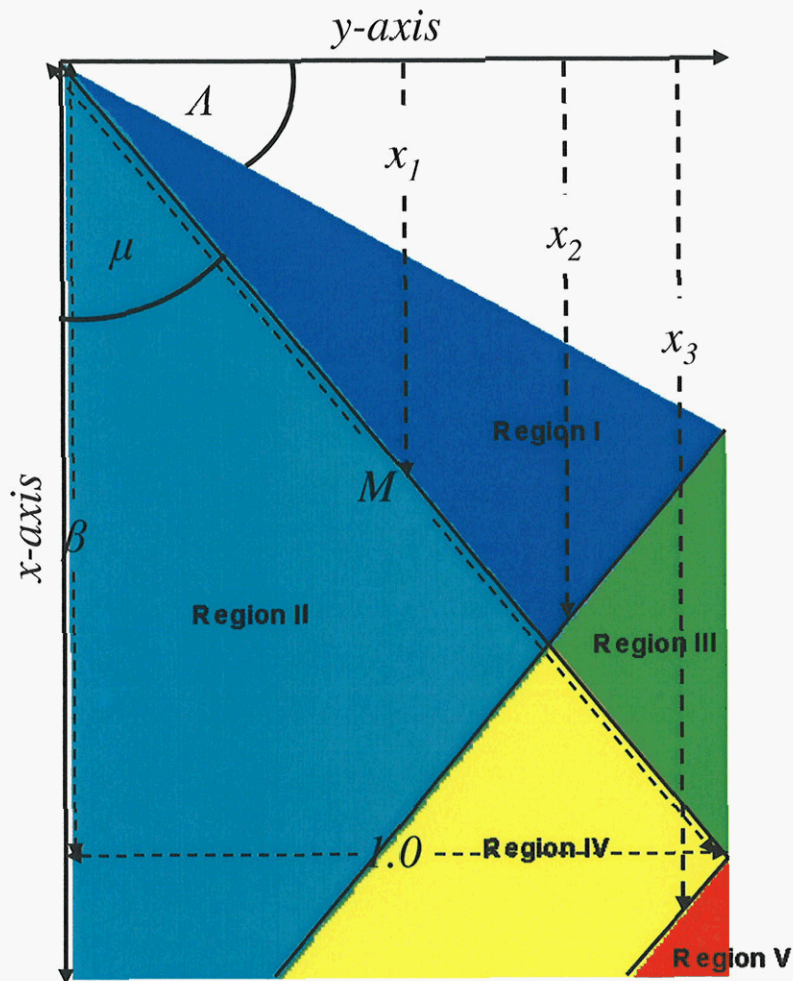
Figure 6. Zoning Rules

8

In order to finalize the new zoning laws, x_1, x_2, and x_3 must be defined as a function of y and z.

$$\beta = \sqrt{M^2 - 1.0} = \frac{1}{\tan \mu} \tag{9}$$

$$x_1 = \beta\sqrt{y^2 + z^2} \tag{10}$$

$$x_2 = \tan \Lambda + \beta\sqrt{(1.0 - y)^2 + z^2} \tag{11}$$

$$x_3 = \beta + \beta\sqrt{(1.0 - y)^2 + z^2} \quad . \tag{12}$$

The Mach cones and WAF surface intersections are represented in Figure 7 by 3-D surfaces.
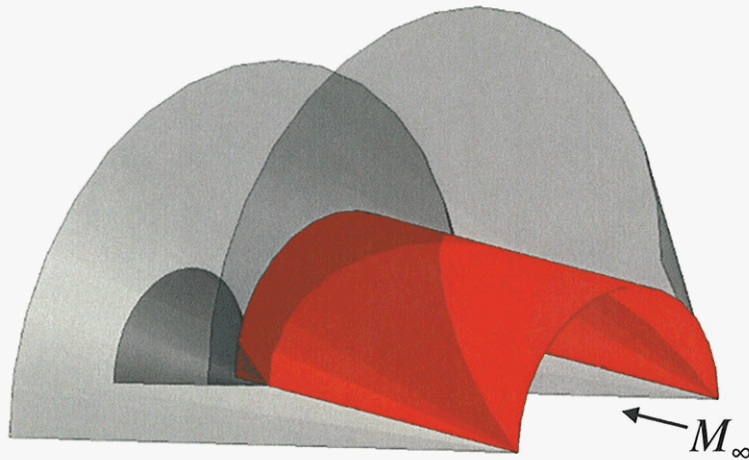
Figure 7. 3-D Surface Intersection

In order to validate the equations used to zone the control points on the fin, the results at Mach 1.6 for a rectangular fin with a chord of 4.25 inches and a span of 3.0 inches at various angles of curvature are compared to the 3-D Computer Aided Design (CAD) model. Figures 8 through 12 show that the code results match the top-view of the CAD model (Fig. 7) for various angles of curvature.
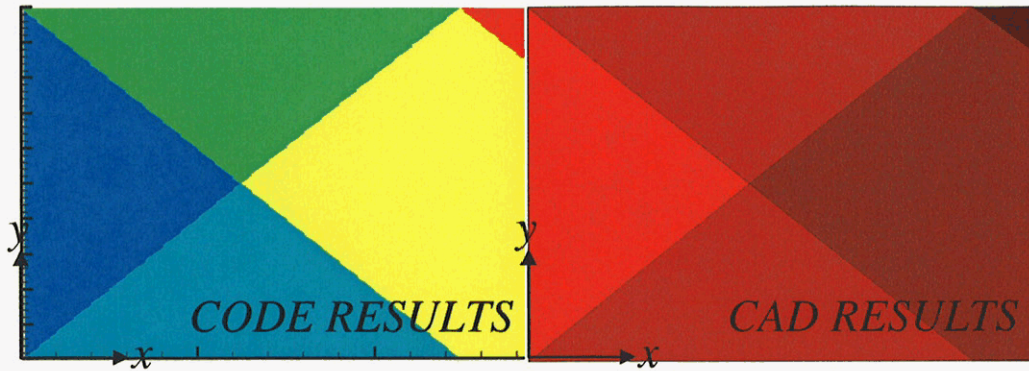
Figure 8. Zoning Verification at Mach 1.6 for 0.0 Degrees of Curvature
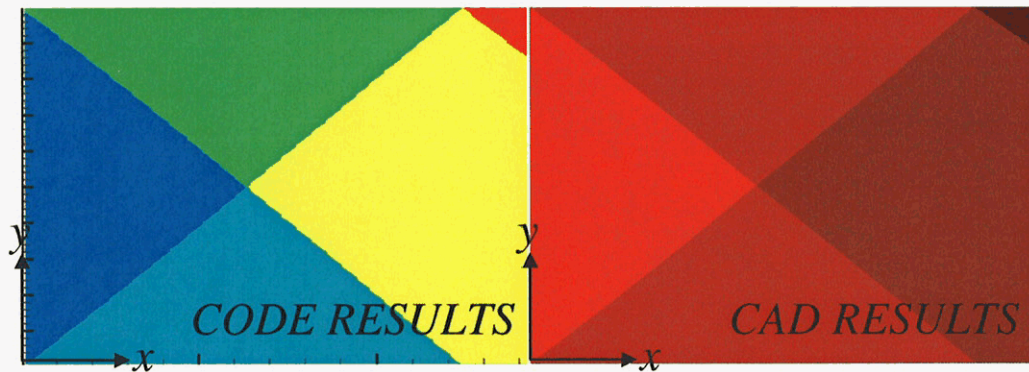

Figure 9. Zoning Verification at Mach 1.6 for 45.0 Degrees of Curvature
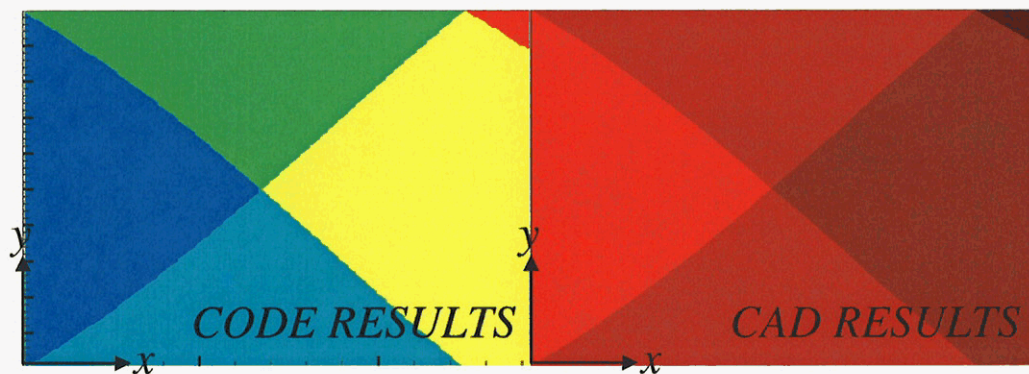

Figure 10. Zoning Verification at Mach 1.6 for 90.0 Degrees of Curvature
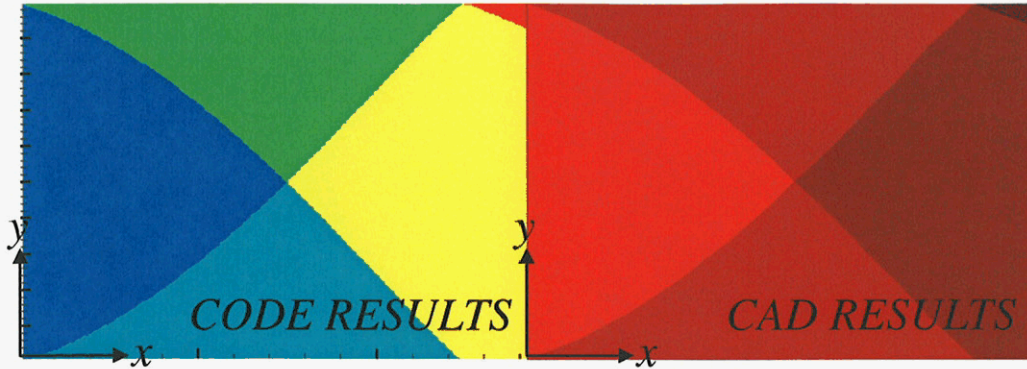
Figure 11. Zoning Verification at Mach 1.6 for 135.0 Degrees of Curvature
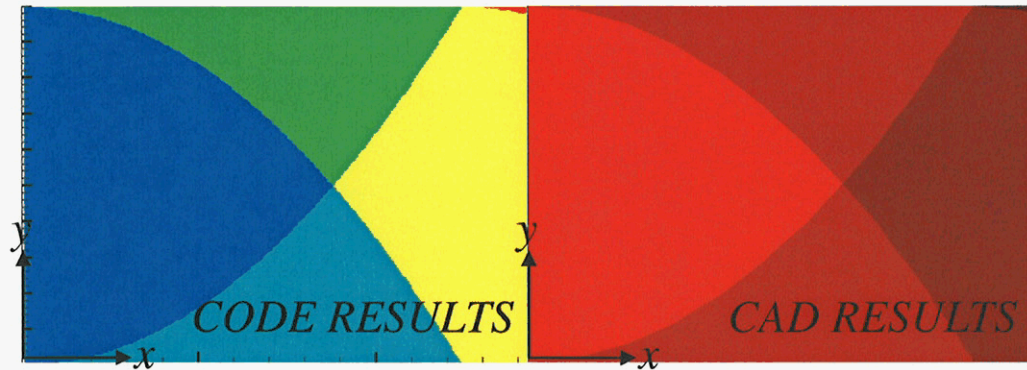
Figure 12. Zoning Verification at Mach 1.6 for 180.0 Degrees of Curvature

C.   Pressure Differential in Each Region of Flow

Now that the fin has been divided into zones based on regions of influence, the pressure differential between the upper and lower surface can be evaluated based on the types of disturbances that affect each region of the fin. Since the potential equation for a fin in supersonic flow is described by an ordinary second-order differential equation, the laws of superposition apply. Therefore, the pressure differential in each region of the fin is a summation of each upstream disturbance type. Since an induced AoA method is being utilized, the AoA (α) seen in Equations (14) through (25) can be equated to:

$$\alpha = \alpha_{AERODYNAMIC} + \alpha_{INDUCED} \quad . \tag{13}$$

11

1. Region I

Region I is the fundamental portion of the fin which lies outside both Mach cones; therefore, control points within Region I are only exposed to infinite fin (airfoil) type disturbances. From linearized supersonic flow theory, the pressure coefficient on the upper surface of a flat plate is given by:

$$C_{p,lower} = \frac{2\alpha}{\sqrt{M^2 - 1}} \tag{14}$$

and

$$C_{p,upper} = -\frac{2\alpha}{\sqrt{M^2 - 1}} \ . \tag{15}$$

Differencing the lower and upper pressure coefficients yield a differential pressure coefficient of:

$$\Delta C_p = \frac{4\alpha}{\sqrt{M^2 - 1}} \tag{16}$$

The pressure differential in Region I using Evvard's theory is based on linearized theory; however, the leading edge sweep angle is included such that:

$$\Delta C_{p,I} = \frac{4\alpha}{\sqrt{\beta^2 - \tan^2 \Lambda}} \ . \tag{17}$$

2. Region II

Region II is located within the interior Mach cone that is produced by the leading edge discontinuity at the root of a swept fin; therefore, it is referred to in text as the triangular fin region. Since there is no discontinuity at the root of a rectangular fin ($\Lambda = 0$), the triangular fin term is null, and Equation (18) reduces to Equation (17). Appropriately, the triangular fin effect increases with sweep angle. The pressure differential in Region II is defined as:

$$\Delta C_{p,II} = \frac{4\alpha}{\pi\sqrt{\beta^2 - \tan^2 \Lambda}} \left[\cos^{-1} \frac{\tan \Lambda + \beta T}{T \tan \Lambda + \beta} + \cos^{-1} \frac{\tan \Lambda - \beta T}{\beta - T \tan \Lambda} \right] \tag{18}$$

where,

$$T = \beta \frac{y}{x} \ . \tag{19}$$

3. Region III

Region III is located within the exterior Mach cone that is produced by the leading edge fin tip; therefore, it is referred to in text as the fin tip region. Since a pressure differential cannot be maintained at the tip of a fin, the potential flow equation is solved with a boundary condition imposed such that the pressure differential at the tip of the fin is zero. Region III is downstream of Region I; therefore, the tip effect is an addition to the infinite fin solution. Since the tip effect uses the tip of the fin as a reference, a coordinate system is defined at the leading edge fin tip such that:

$$x_{tip} = x - \tan \Lambda \tag{20}$$

$$y_{tip} = y - 1.0 \quad . \tag{21}$$

With the tip coordinates defined, the pressure differential coefficient due to the fin tip disturbances can be written as:

$$\Delta C_{p,tip} = -\frac{4\alpha}{\pi \sqrt{\beta^2 - \tan^2 \Lambda}} \left[\cos^{-1} \frac{-\left[x_{tip} + y_{tip} \left(2\beta + \tan \Lambda \right) \right]}{x_{tip} - y_{tip} \tan \Lambda} \right] \quad . \tag{22}$$

The pressure differential in Region III can be expressed as:

$$\Delta C_{p,III} = \Delta C_{p,I} + \Delta C_{p,tip} \quad . \tag{23}$$

4. Region IV

Region IV is the area within the interior and exterior Mach cones; therefore, Region IV is affected by infinite fin disturbances, triangular fin disturbances, and fin tip disturbances. Since each of these types of disturbances have been defined, the pressure differential in Region IV is simply:

$$\Delta C_{p,IV} = \Delta C_{p,II} + \Delta C_{p,tip} \quad . \tag{24}$$

5. Region V

In some swept fin cases, the Mach cone originating from the root leading edge discontinuity intersects the fin tip; in which case, an addition Mach cone is created with an origin at the fin tip intersection. Thus, the fifth fin region is formed within Region IV designated as Region V. Region V is the result of a combination of Region IV disturbances with an additional tip effect to yield a pressure differential defined as:

$$\Delta C_{p,V} = \frac{4\alpha}{\pi \sqrt{\beta^2 - \tan^2 \Lambda}} \left[\cos^{-1} \frac{x_{tip} - y_{tip} \left(\tan \Lambda - 2\beta \right) + 2 \tan \Lambda}{x_{tip} + \left(y_{tip} + 2 \right) \tan \Lambda} \right] \quad . \tag{25}$$

A summary of the pressure coefficients for each region in presented in Table 2.

Table 2. Pressure Differential Due to AoA

Region	Region Conditional	Pressure Coefficient Differential
I	$x < x_1$ and $x < x_2$	$$\Delta C_{p,I} = \frac{4\alpha}{\sqrt{\beta^2 - \tan^2 \Lambda}}$$
II	$x > x_1$ but $x < x_2$	$$\Delta C_{p,II} = \frac{4\alpha}{\pi\sqrt{\beta^2 - \tan^2 \Lambda}}\left[\cos^{-1}\frac{\tan\Lambda + \beta T}{T\tan\Lambda + \beta} + \cos^{-1}\frac{\tan\Lambda - \beta T}{\beta - T\tan\Lambda}\right]$$
III	$x > x_2$ but $x < x_1$	$$\Delta C_{p,III} = \Delta C_{p,I} + \Delta C_{p,tip}$$
IV	$x > x_1$ and $x > x_2$ but $x < x_3$	$$\Delta C_{p,IV} = \Delta C_{p,II} + \Delta C_{p,tip}$$
V	$x > x_3$	$$\Delta C_{p,V} = \frac{4\alpha}{\pi\sqrt{\beta^2 - \tan^2 \Lambda}}\left[\cos^{-1}\frac{x_{tip} - y_{tip}(\tan\Lambda - 2\beta) + 2\tan\Lambda}{x_{tip} + (y_{tip} + 2)\tan\Lambda}\right]$$

D. Empirically Derived Induced AoA

In order to develop an empirical expression to describe the induced forces and moments generated by fin curvature, the test data collected at the January 2005 LMMFC HSWT was thoroughly analyzed to find a correlation. In this particular test, the fins were mounted on a splitter-plate to minimize the appearance of shock waves upstream of the fins. Figure 13 shows one of the WAFs mounted on the splitter-plate along with the test sign convention.

14
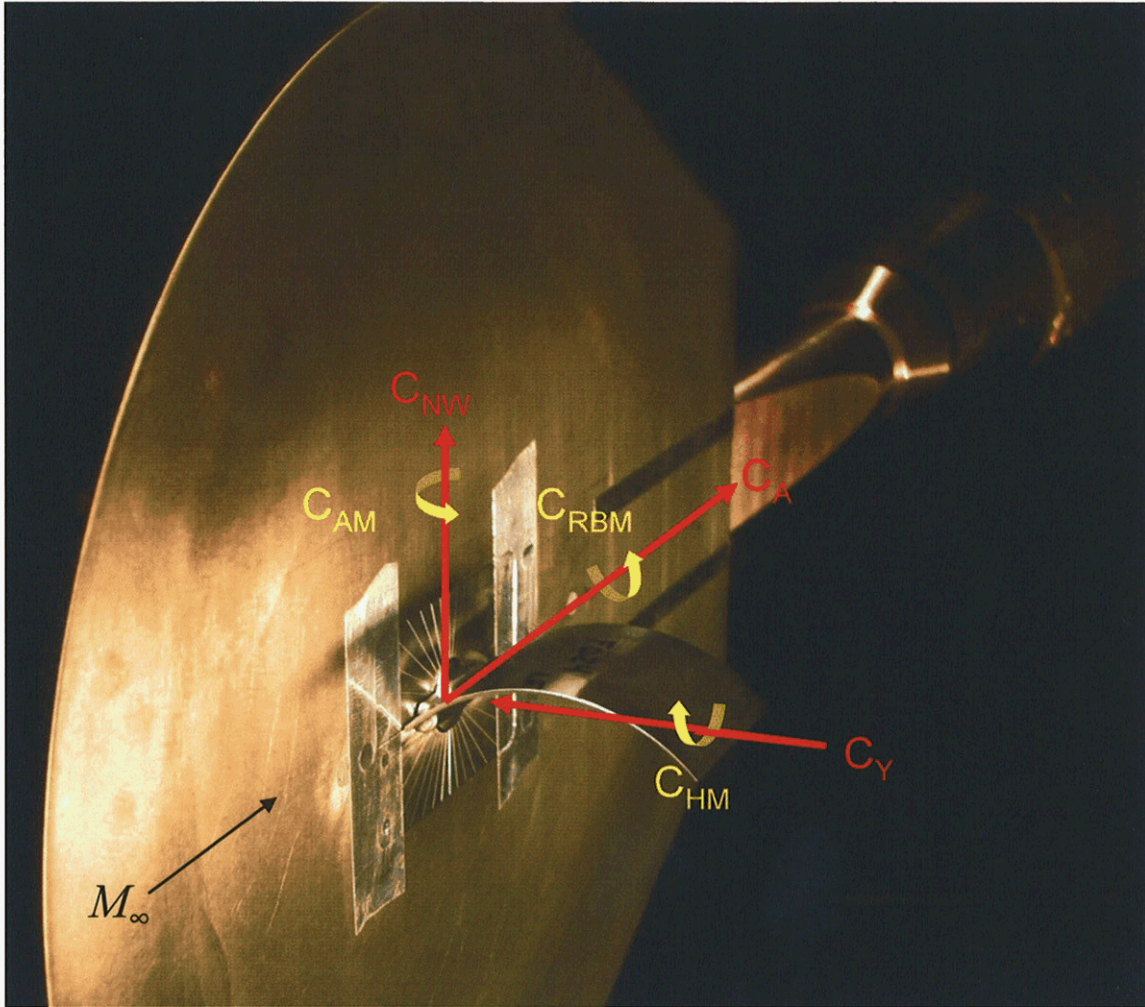
Figure 13. WAF on Splitter-Plate with Sign Convention

In order to obtain an empiral relationship, the induced AoA of the three different aspect ratio families was plotted at different supersonic Mach numbers. A linear curve-fit was used to investigate a correlation between the angle of curvature and the induced AoA. Figures 14 through 16 show the linear relationship of the three aspect ratio fins.
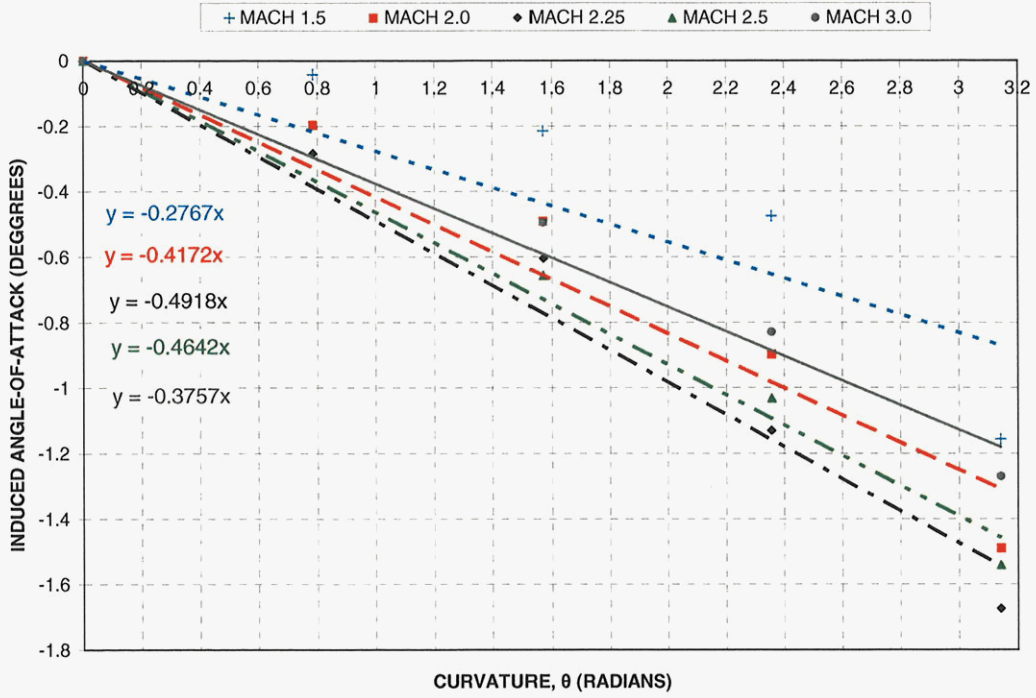
Figure 14. Curvature Effects for AR = 1.4118
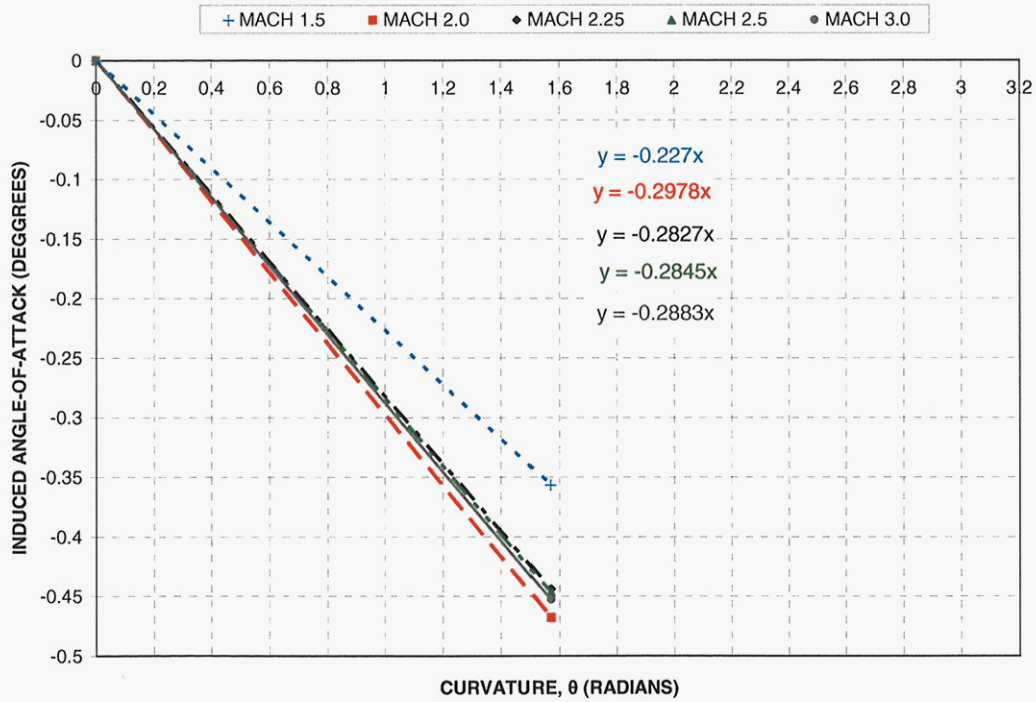

Figure 15. Curvature Effects for AR = 1.8824
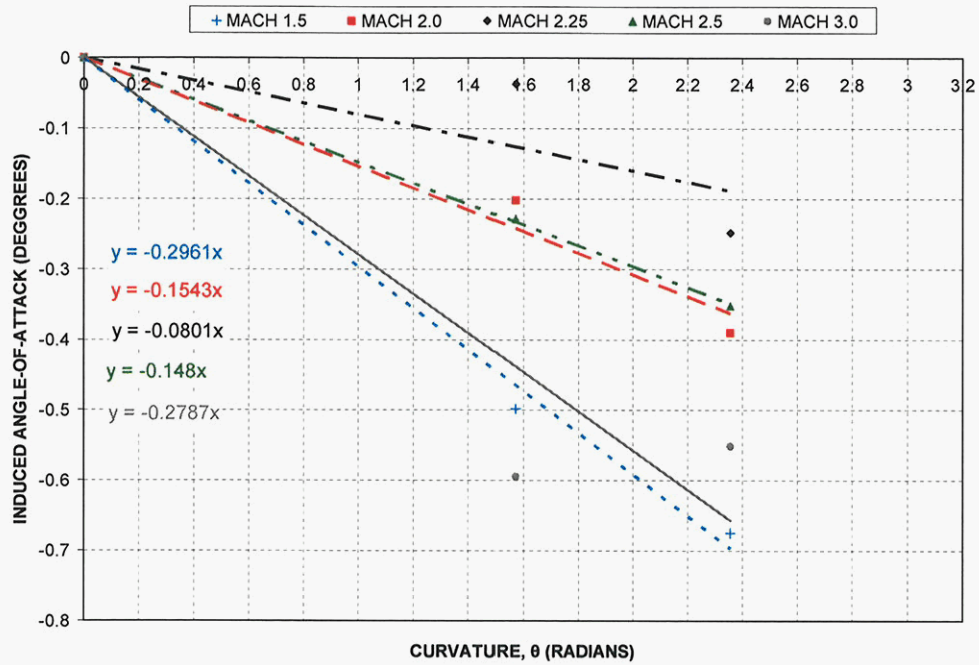
Figure 16. Curvature Effects for AR = 2.8333

The slopes from the linear fits (Figs. 14 through 16) were then plotted with respect to aspect ratio at each Mach number. While the resulting plots varied with Mach number, the aspect ratio effects were matched well with a power series expression for each Mach number. Figure 17 shows the aspect ratio dependence of the slope at Mach 2.25.
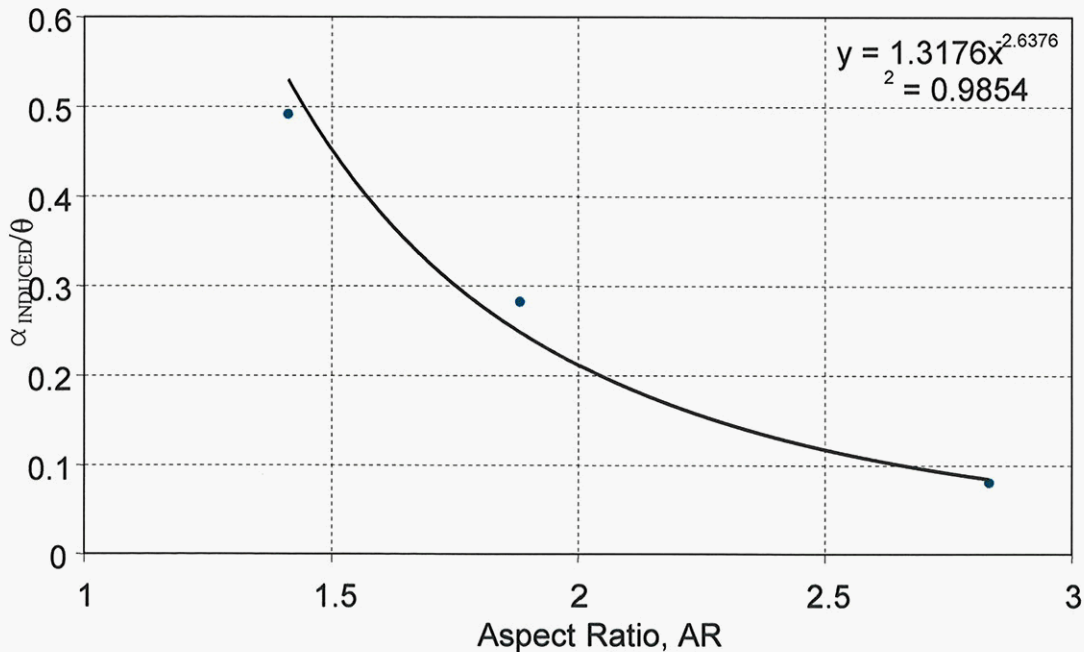

Figure 17. Aspect Ratio Dependence at Mach 2.25

Up to this point in the analysis, only a small amount of the collected data had been analyzed to find a correlation. Therefore, the next step was to include all the data in the correlation. The results from the test data were tabulated with respect to curvature, aspect ratio, Mach number, and induced AoA. In order to capture the Mach dependency, a genetic algorithm was used to find three different power series relationships that could be applied piecewise. A dividing Mach number, also a genetic algorithm variable, would be used to capture any inflection in the data. The three power series relationships are related using a linear interpolation based on Mach number about the dividing Mach number. The induced angles from the test were compared to the correlation, and the genetic algorithm was used to minimize the root squared sum of the differences between the correlation and the test data. A second-order polynomial scheme was also investigated with less success. The power series constants and dividing Mach number chosen by the genetic algorithm and the associated equations are presented below. In Equations (26) through (30), the induced AoA ($\alpha_{INDUCED}$) is represented in degrees, and curvature angle (θ) is represented in radians.

$$a = 0.2425 \cdot \theta \cdot AR^{0.1709} \tag{26}$$

$$b = 1.1583 \cdot \theta \cdot AR^{-2.4181} \tag{27}$$

$$c = 0.4346 \cdot \theta \cdot AR^{-0.4323} \tag{28}$$

For $Mach \geq 2.2630$

$$\alpha_{INDUCED} = c + (b - c) \cdot \frac{3.0 - Mach}{3.0 - 2.2630} \tag{29}$$

For $Mach < 2.2630$

$$\alpha_{INDUCED} = b + (a - b) \cdot \frac{2.2630 - Mach}{2.2630 - 1.5} \quad . \tag{30}$$

As seen in Figures 18 and 19, the correlation worked well. The induced AoA tends to have an inflection point near Mach 2.25. The dividing Mach number helps the correlation capture the inflection of the data. The overall performance of the correlation is seen in Figure 19. While the correlated induced AoA is not quite within the uncertainty of the measured induced AoA (+- 0.1-degree), the correlation was assumed to be adequate to proceed with the methodology.
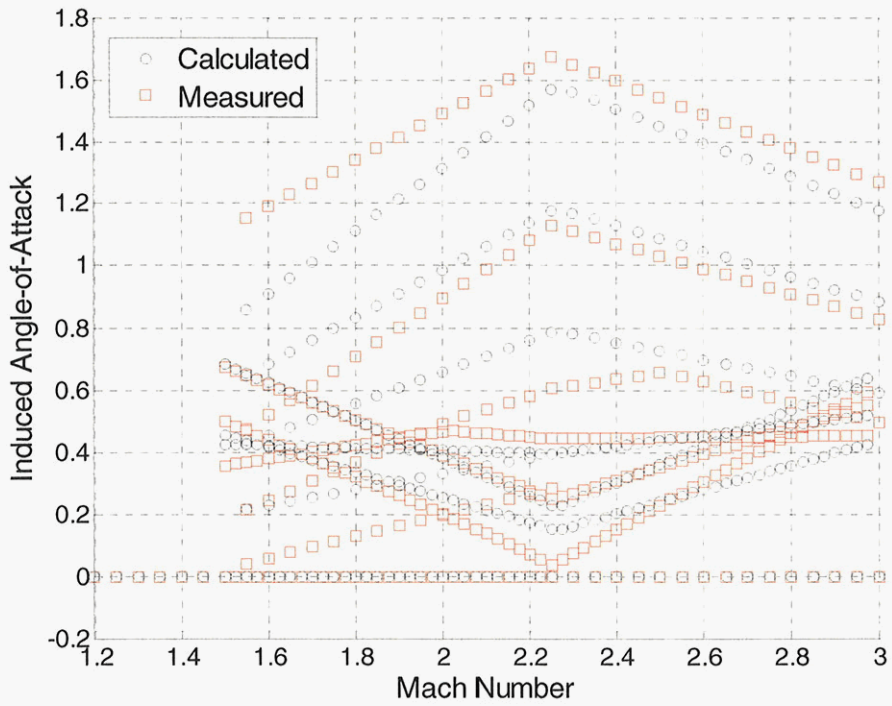
*Figure 18. Correlated Induced AoA Versus Mach Number*
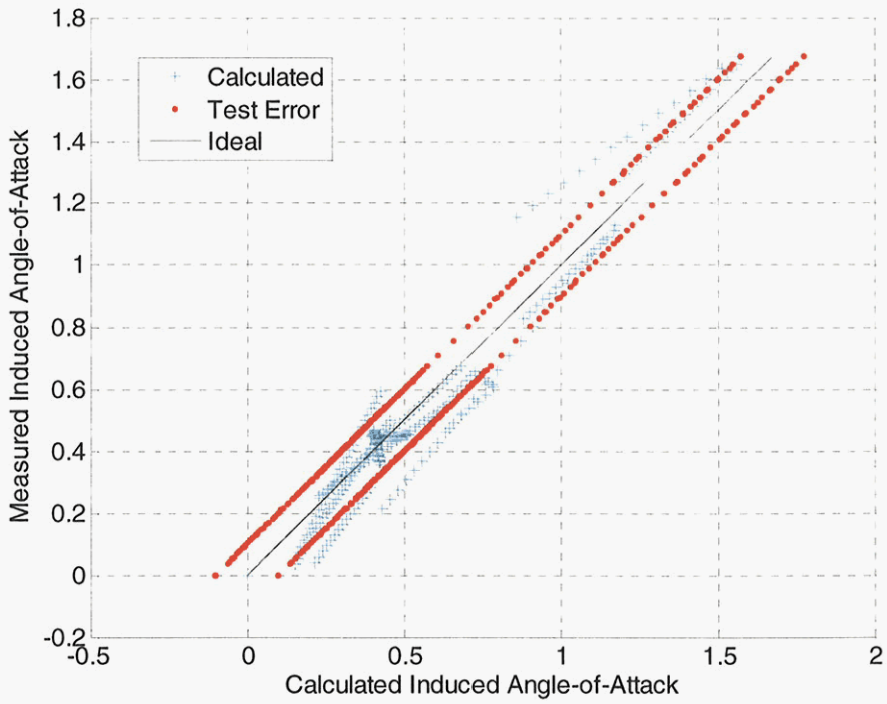
Figure 19. Measured Versus Correlated Induced AoA

IV. INTEGRATION OF THE PRESSURE DISTRIBUTION

Using the induced AoA in conjunction with the modified form of Evvard's theory results in a method of predicting the induced and AoA dependent pressure loading on a WAF. In order to obtain the force and moment coefficients, the pressure differentials must be numerically integrated over the WAF surface.

The aerodynamic loads exerted on the fin are a product of the differential pressure coefficient and the appropriate fin area. The normal force and side force are based on the area of the fin projected onto the xy-plane and the xz-plane, respectively. The moments are a summation of the product of the incremental forces and their respective distances to the reference location. The root bending moment is referenced about the root, and the hinge moment is referenced about the leading edge. The forces and moments can be expressed as:

$$\Delta A_{x,y} = \Delta x \cdot \Delta y \tag{31}$$

$$C_N = \frac{1}{S_{REF}} \sum_{i=1}^{NP} \Delta C_{P_i} \cdot \Delta A_{x,y_i} \tag{32}$$

$$C_{HM} = \frac{1}{S_{REF} \cdot L_{REF}} \sum_{i=1}^{NP} \Delta C_{P_i} \cdot \Delta A_{x,y_i} \cdot x_i \tag{33}$$

$$C_Y = \frac{1}{S_{REF}} \sum_{i=1}^{NP} \Delta C_{P_i} \cdot \Delta x_i \cdot \Delta z_i \tag{34}$$

$$C_Y = \frac{1}{S_{REF}} \sum_{i=1}^{NP} \Delta C_{P_i} \cdot \Delta x_i \cdot \Delta y_i \cdot \left(\frac{dz}{dy}\right)_i \tag{35}$$

$$C_Y = \frac{1}{S_{REF}} \sum_{i=1}^{NP} \Delta C_{P_i} \cdot \Delta A_{x,y_i} \cdot \tan \delta_i \tag{36}$$

$$C_{RBM} = \frac{1}{S_{REF} \cdot L_{REF}} \left[\sum_{i=1}^{NP} \Delta C_{P_i} \cdot \Delta A_{x,y_i} \cdot y_i + \sum_{i=1}^{NP} \Delta C_{P_i} \cdot \Delta A_{x,y_i} \cdot \tan \delta_i \cdot z_i \right] . \tag{37}$$

V. RESULTS

The results of applying the induced AoA to Evvard's theory modified for fin curvature show good agreement at both positive and negative AoA. The results are presented in two segments: (1) selective plots comparing theoretical results and test data as a function of AoA and, (2) pressure differential contours at 5 degrees of incidence on selective fins. The normal force, side force, root bending moment, and hinge moment will be compared to test data with respect to AoA. Since the focus is on the pressure-driven forces and moments, the axial force and associated axial moment will be neglected in the results.

A.   Comparison to Test Data

Each plot contains data for various angles of curvature from both the methodology and from the splitter-plate test data. The theoretical solution is represented as a line (dotted, dashed, and solid). The test results are represented as various symbols denoted in the legend on each chart along with the word "Test." The test data represents both viscous and inviscid effects, while the theoretical solution only models the inviscid effects. One source of discrepancy between the theoretical solution and the test results is the thickness of the fins. Theoretically, the fins are infinitely thin. In addition to a finite thickness, the test fins have an increased thickness near the root for required structural properties (Fig. 2). The test data uncertainty as quoted by LMMFC HSWT can be seen in Table 3, and is shown on select coefficients in Figures 20 through 59. In most cases, the size of the error band is smaller than the data symbol.

Table 3. Coefficient Uncertainty

uCN	uCY	uCHM	uCRBM
$\pm$ 0.0055	$\pm$ 0.0020	$\pm$ 0.0055	$\pm$ 0.0025

1.   Normal Force

Figures 20 through 29 show the comparison of the theoretical normal force and the test results. Overall, the addition of the curvature term in the zoning laws allows Evvard's theory to model the changes in the normal force slope extremely well (within the uncertainty of the test data). The normal force slope of the moderate aspect ratio (AR = 1.4118 and AR = 1.8824) fins are modeled slightly better than the extreme aspect ratio fins. For the higher aspect ratio cases (AR = 2.8333) (Figs. 26 through 28) the normal force slope appears to be slightly different at positive versus negative AoA. Evvard's theory works well at Mach 1.5, but the accuracy seems to improve with increasing Mach number. As for the induced normal force, the empirical fit for the induced AoA allows the normal force to match the test data at low AoA. The largest discrepancy in the low incidence normal force modeling is seen in Figure 20 for a fin curvature of 180 degrees. Even though leading edge sweep angle was not accounted for in the empirical fit, Figure 29 shows good agreement between theory and test data for a leading edge sweep angle of 35 degrees.
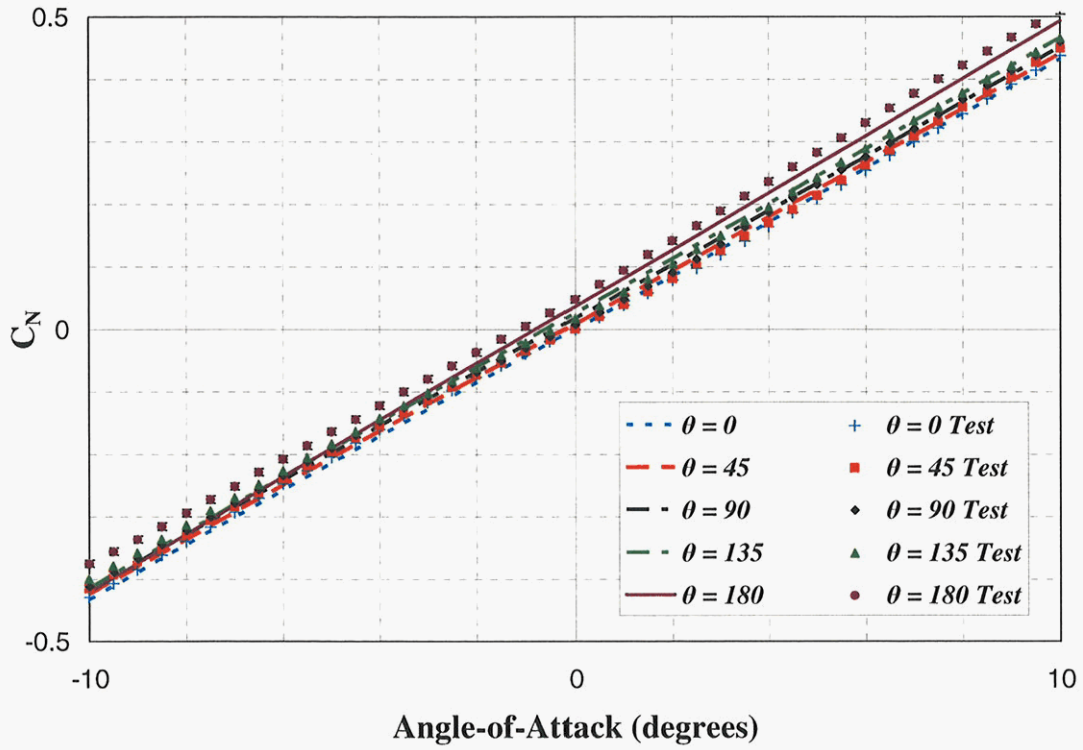
*Figure 20. Normal Force Comparison for AR = 1.4118 at Mach 1.5*
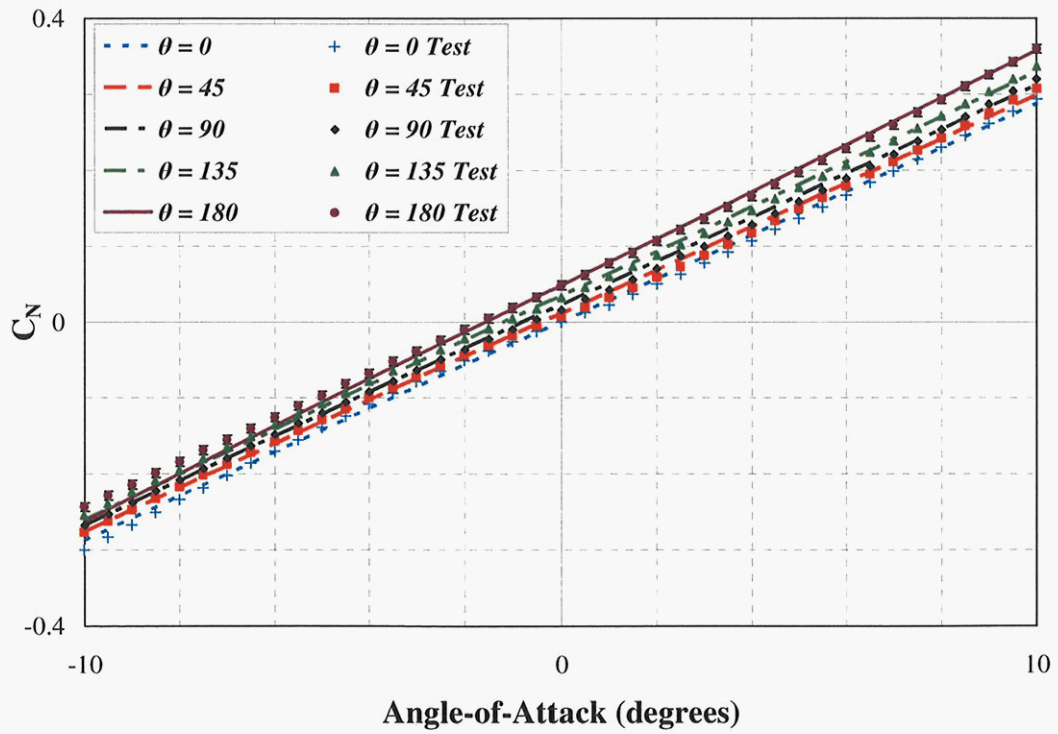
*Figure 21. Normal Force Comparison for AR = 1.4118 at Mach 2.25*
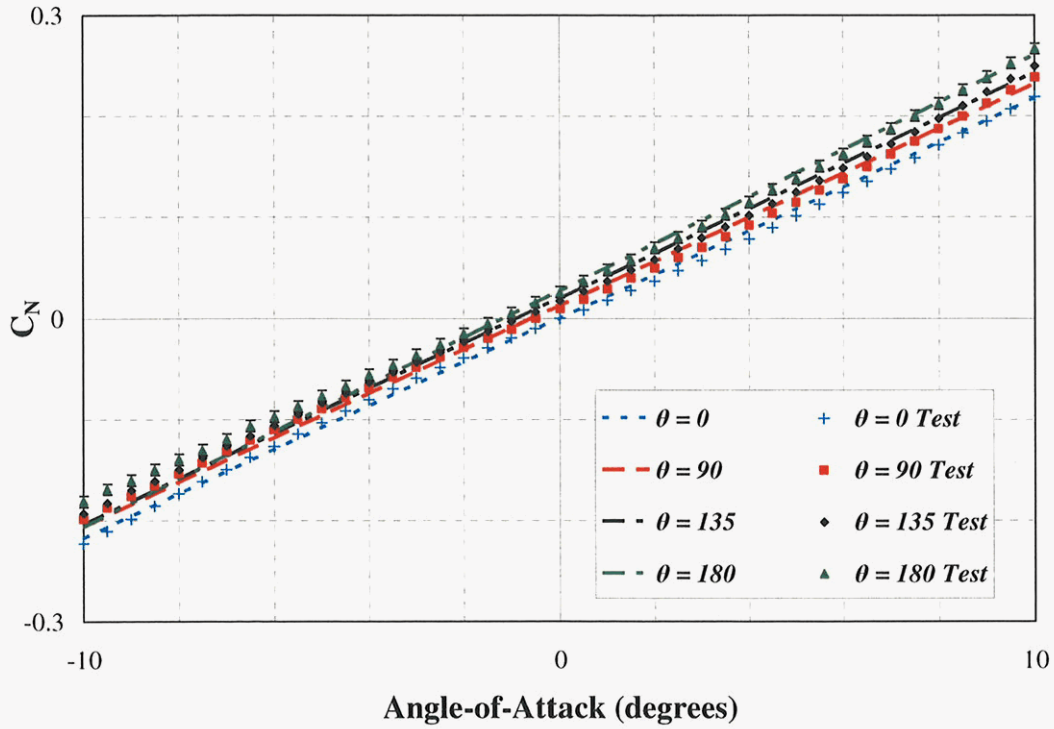
*Figure 22. Normal Force Comparison for AR = 1.4118 at Mach 3.0*
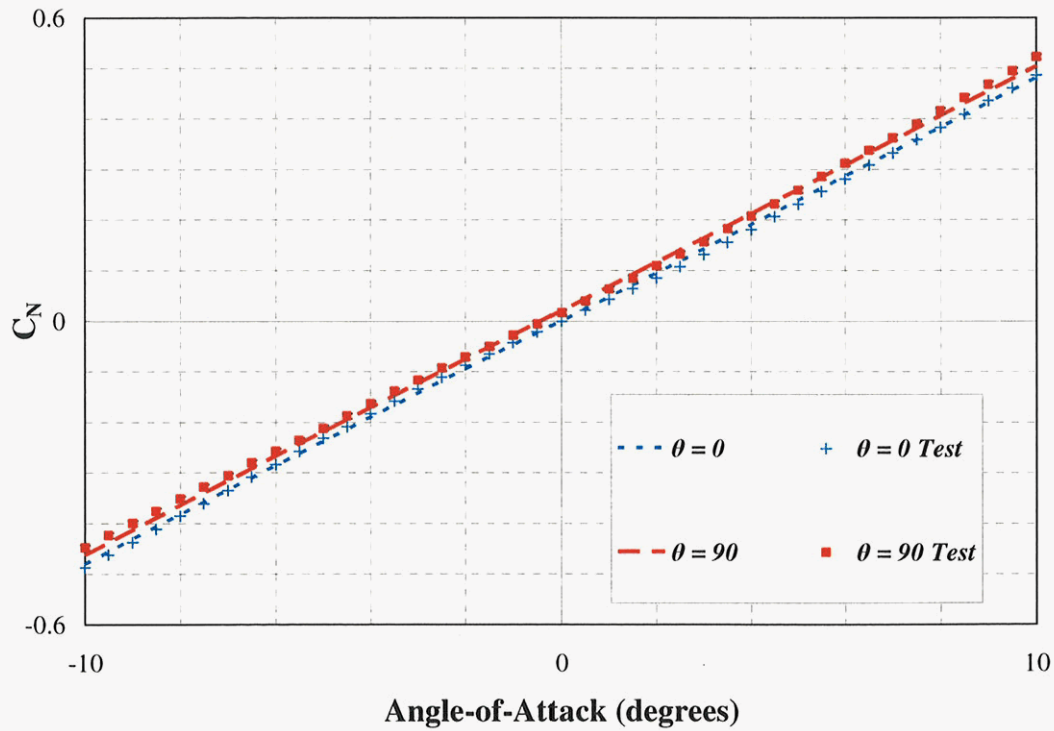
*Figure 23. Normal Force Comparison for AR = 1.8824 at Mach 1.5*
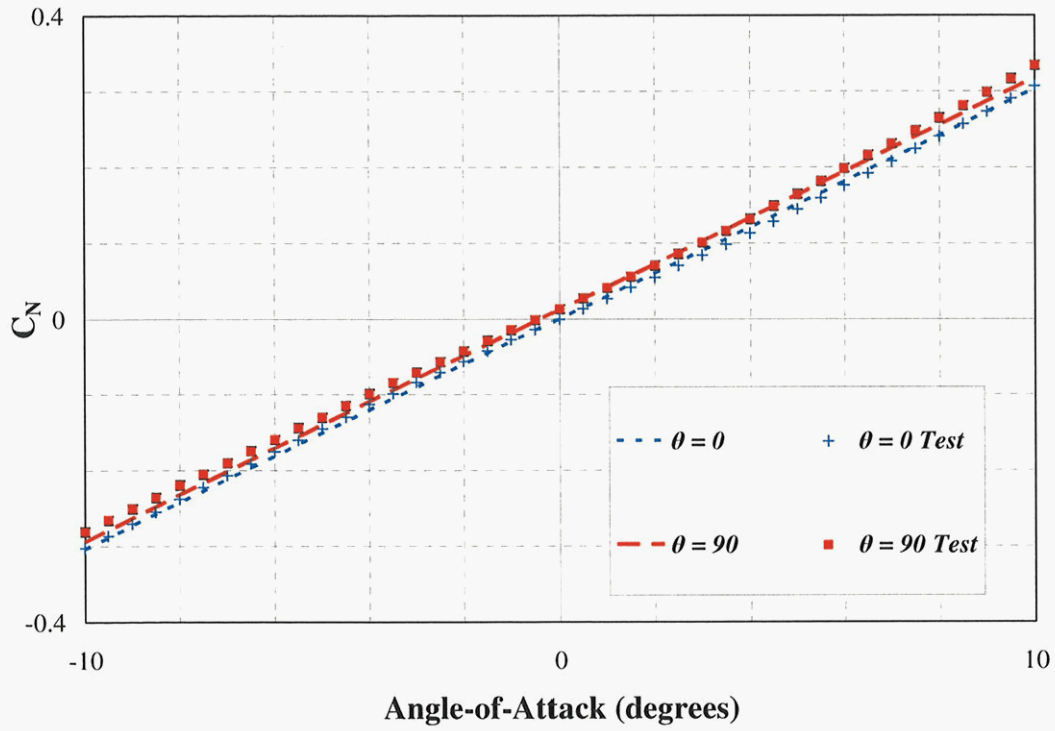
*Figure 24. Normal Force Comparison for AR = 1.8824 at Mach 2.25*
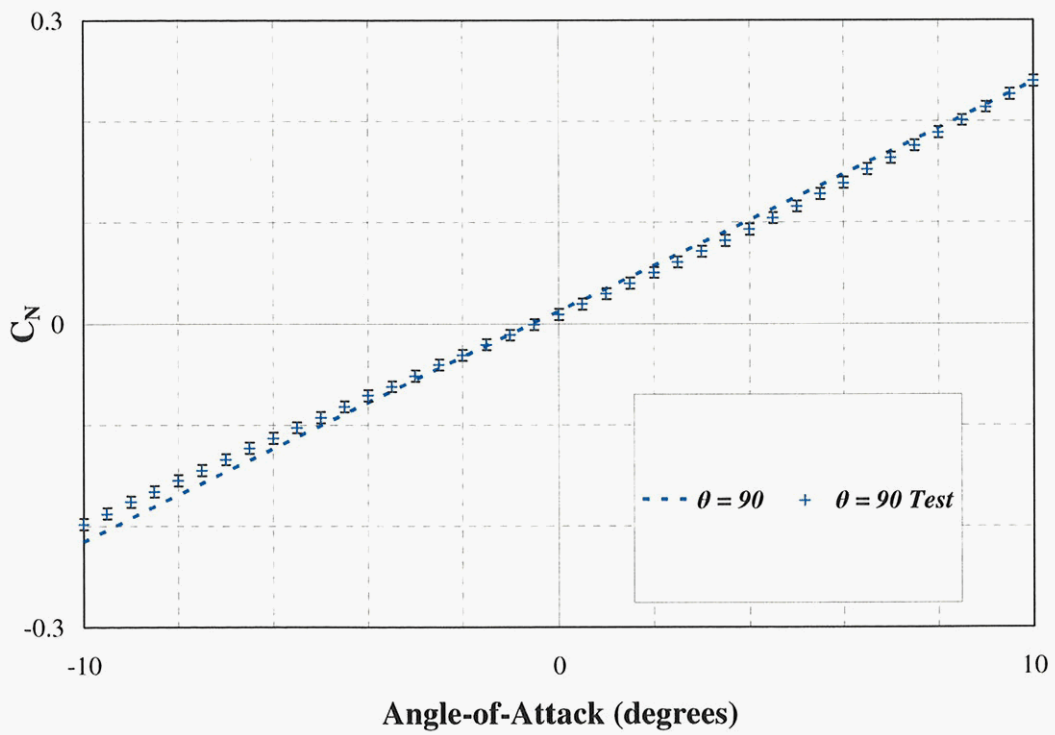
*Figure 25. Normal Force Comparison for AR = 1.8824 at Mach 3.0*

24
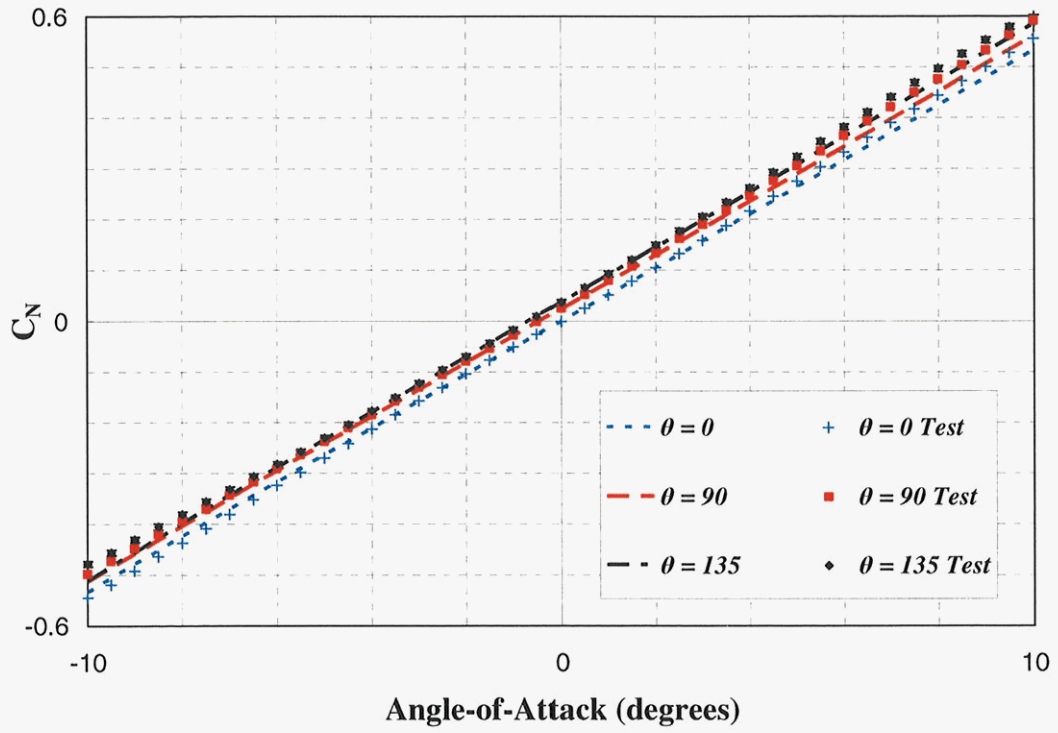
*Figure 26. Normal Force Comparison for AR = 2.8333 at Mach 1.5*
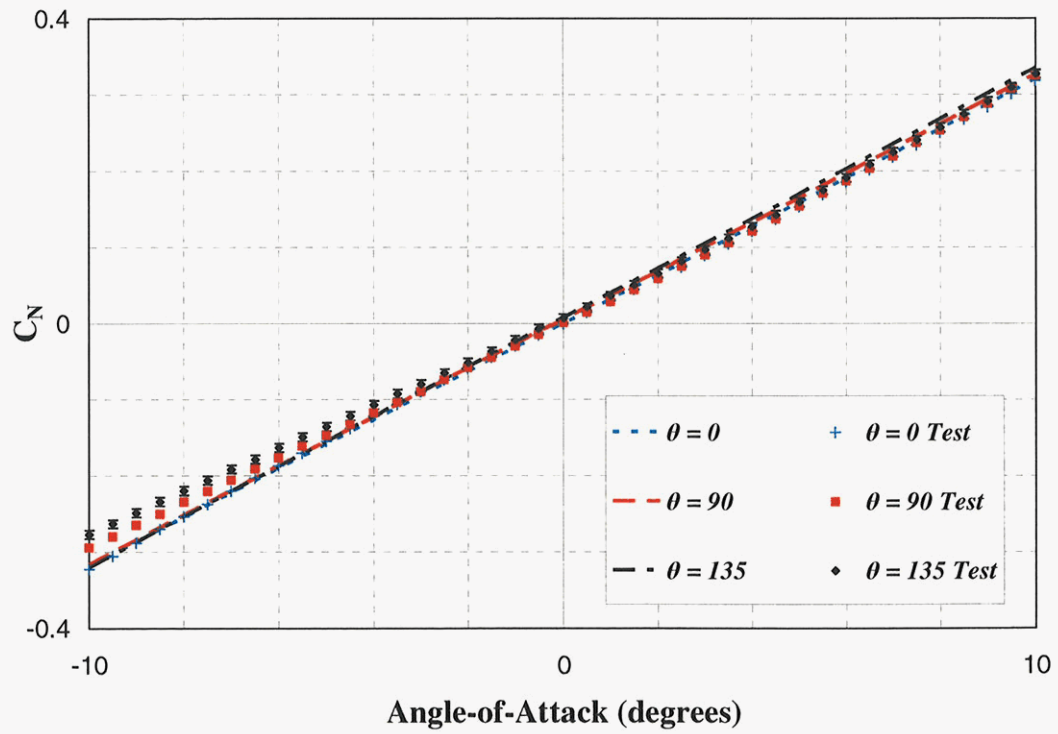
Figure 27. Normal Force Comparison for AR = 2.8333 at Mach 2.25
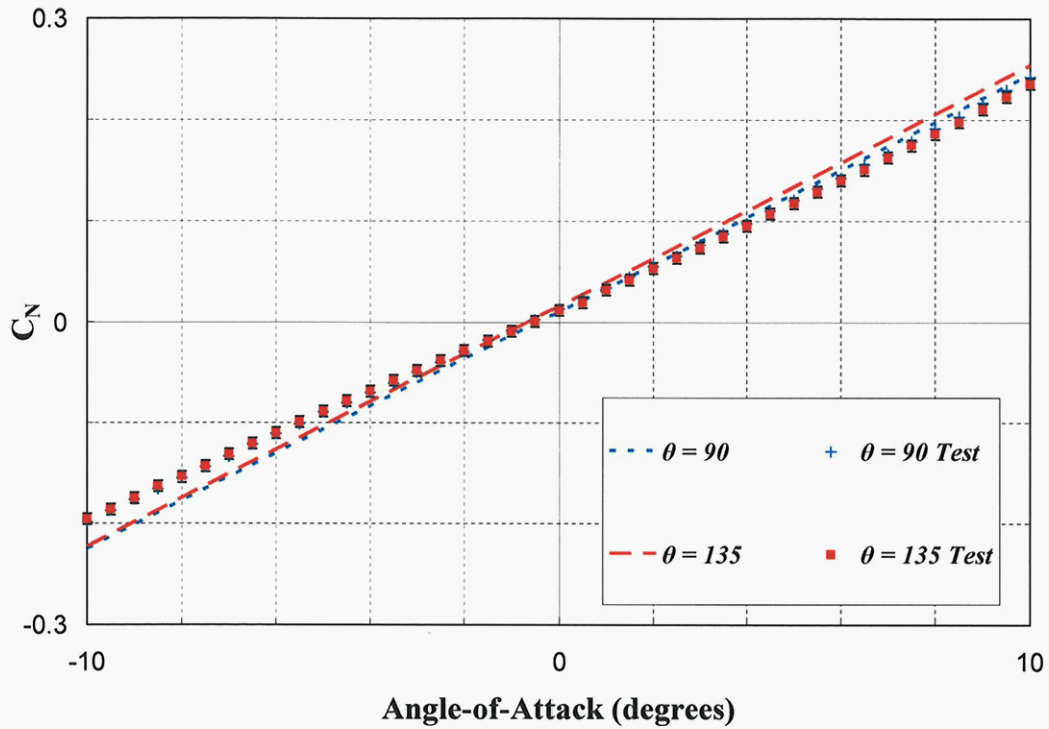
Figure 28. Normal Force Comparison for AR = 2.8333 at Mach 3.0
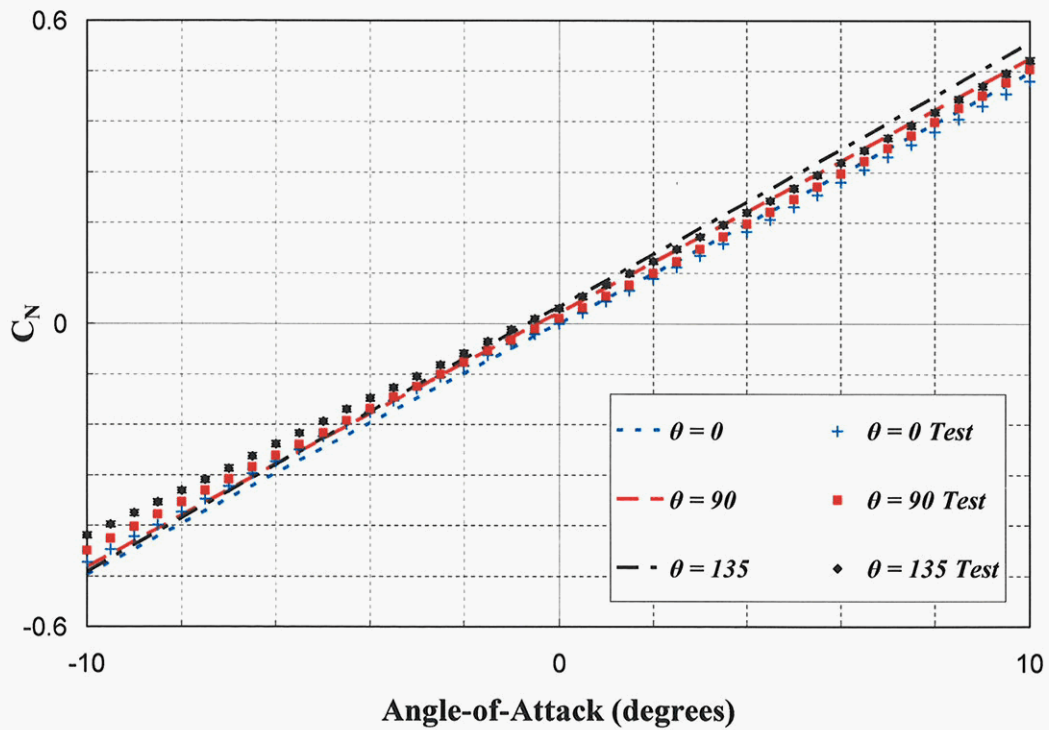
Figure 29. Normal Force for AR = 1.8824; Λ = 35° at Mach 1.5

2. Side Force

The side force of the fin, as seen in Figure 13, is the force that is directed from the fin tip to the root. The pressure contour plots (Figs. 60 through 71) can be used to visualize the manner in which the pressure exerts a side force on the fin. A curved fin has surface area in the xz-plane; therefore, the pressure differential generates a side force on a WAF.

The theoretical solution for all fins and conditions shows a pushing (directed from tip to root) side force at positive AoA and a pulling (directed from root to tip) side force at negative AoA. The test data shows that a pulling force is dominant even at positive AoA. As seen in Figure 2, the tested fins were thickened near the root for structural rigidity, which alters the area of the fin in the xz-plane. In addition to the thickened root, the splitter-plate also is suspected to influence the side force. For finite thickness fin in supersonic flow, the leading edge of the fins will produce a shock wave. On the convex side of the tested WAFs near root, the shock wave is most likely reflected by the splitter-plate forming a region of high pressure. A region of high pressure in this location would generate a pulling side force. Again, the theory does not account for fin thickness. However, the side force order of magnitude and data trend is modeled well. Figures 30 through 39 show the side force coefficient comparison of the theory to the test data. The theory typically over-predicts the magnitude of side force at positive AoA, but matches the magnitude well at negative AoA. The computed side force of the swept fin matches test data remarkably better than the rectangular fins (Fig. 39).
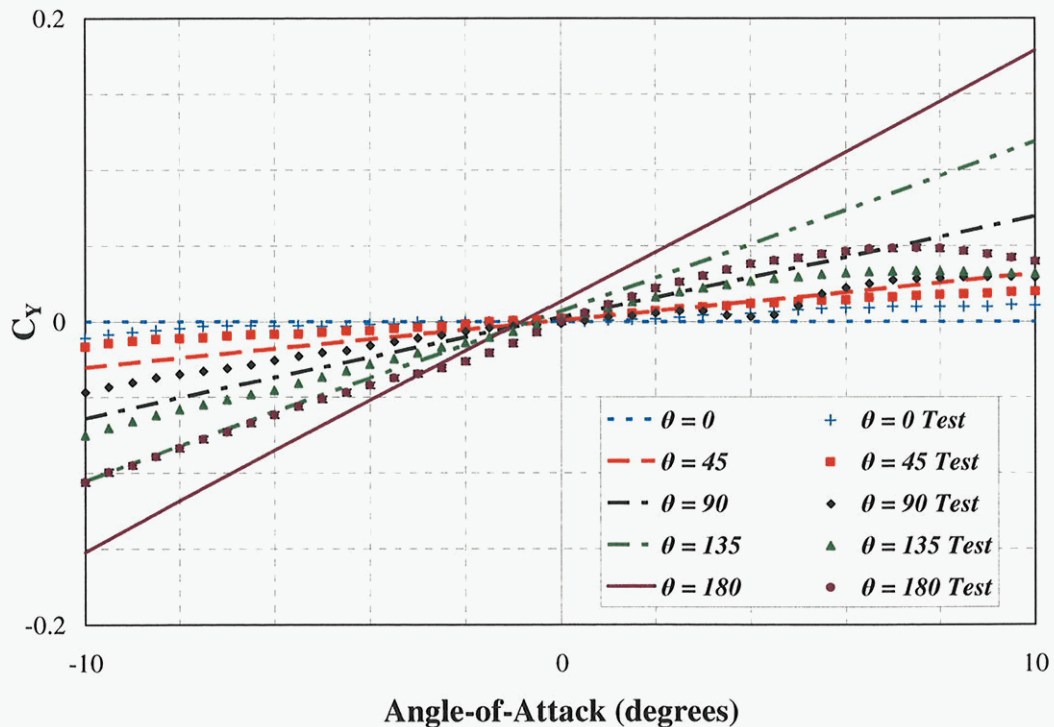

*Figure 30. Side Force Comparison for AR = 1.4118 at Mach 1.5*
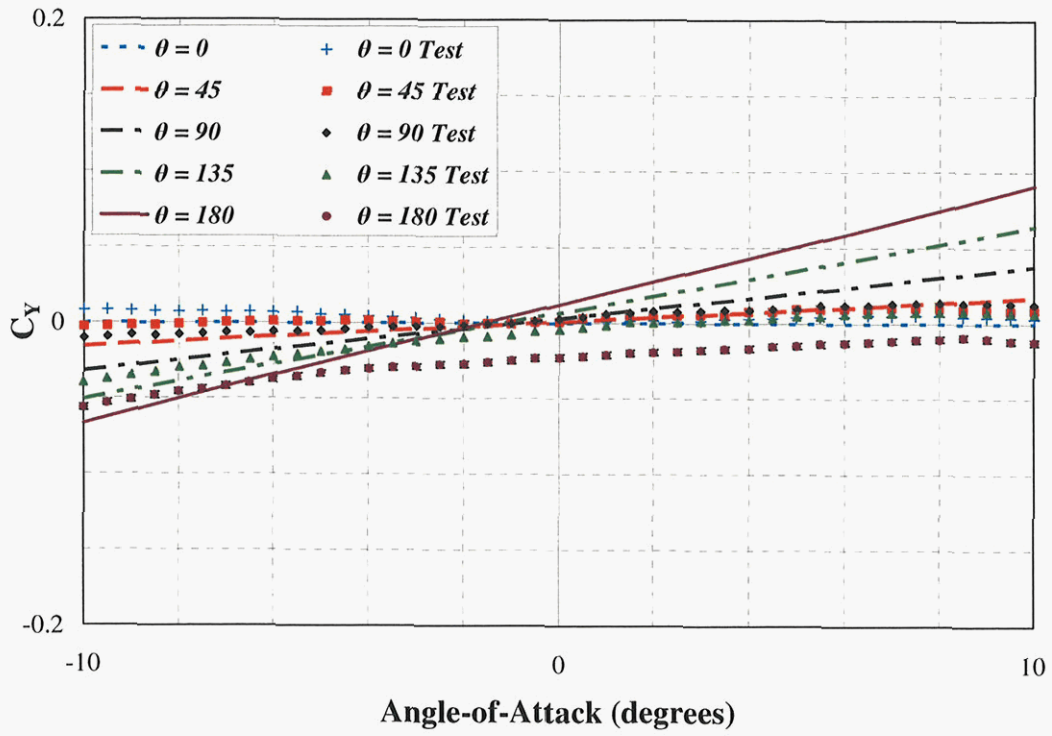
*Figure 31. Side Force Comparison for AR = 1.4118 at Mach 2.25*
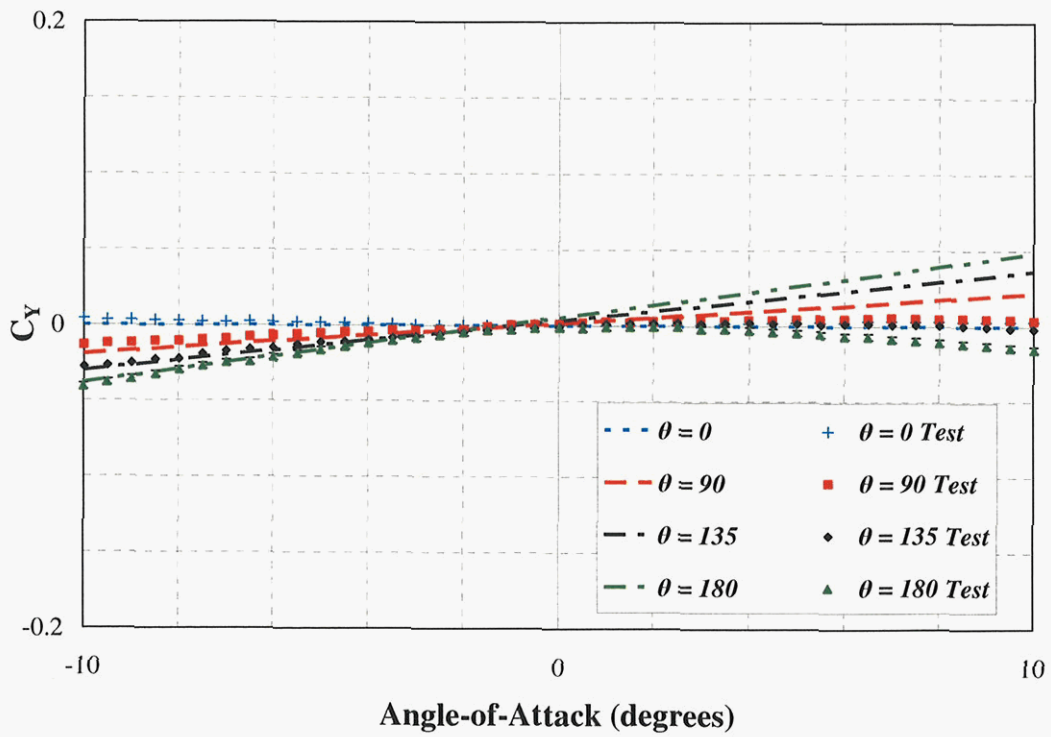
*Figure 32. Side Force Comparison for AR = 1.4118 at Mach 3.0*
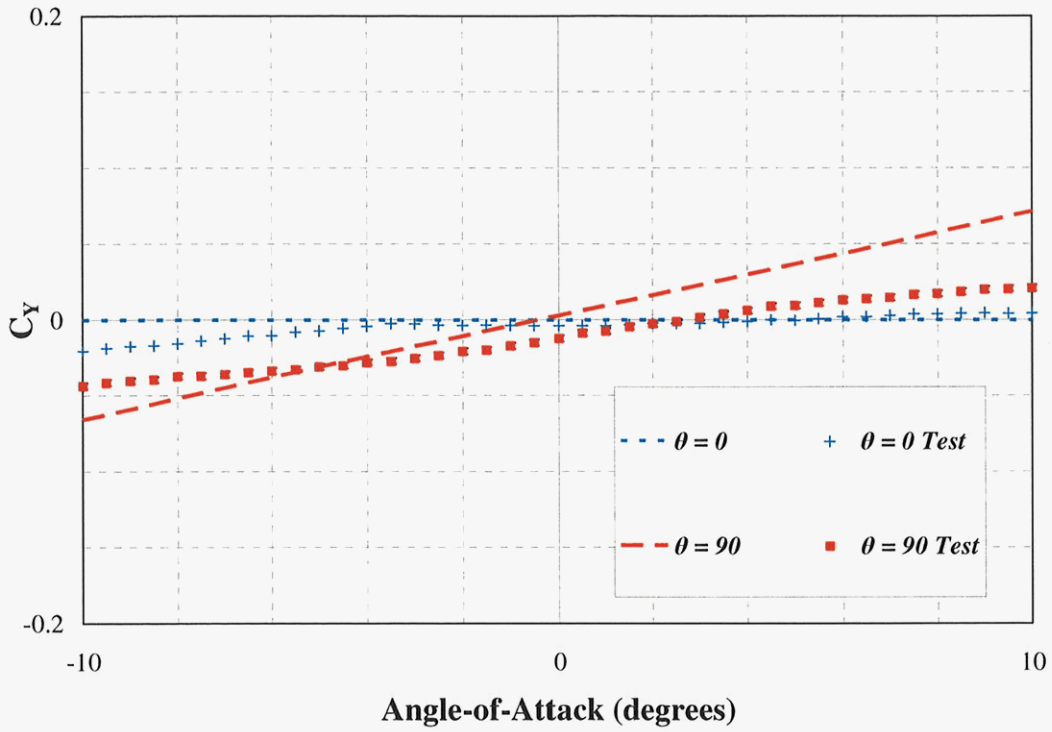
*Figure 33. Side Force Comparison for AR = 1.8824 at Mach 1.5*
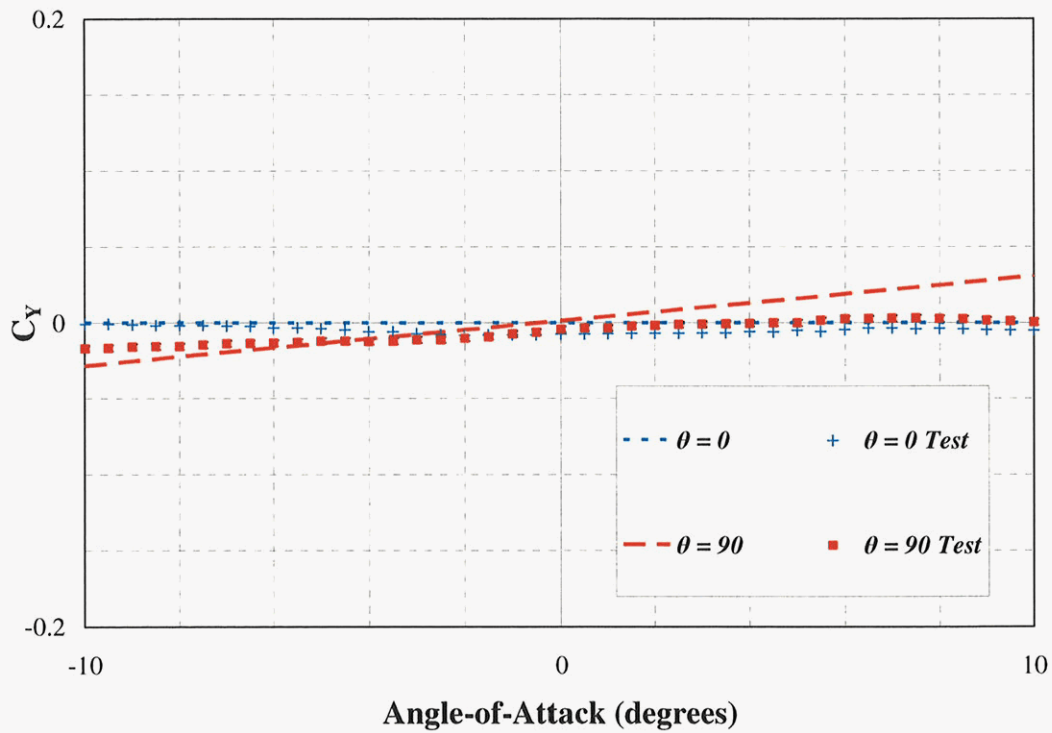
*Figure 34. Side Force Comparison for AR = 1.8824 at Mach 2.25*
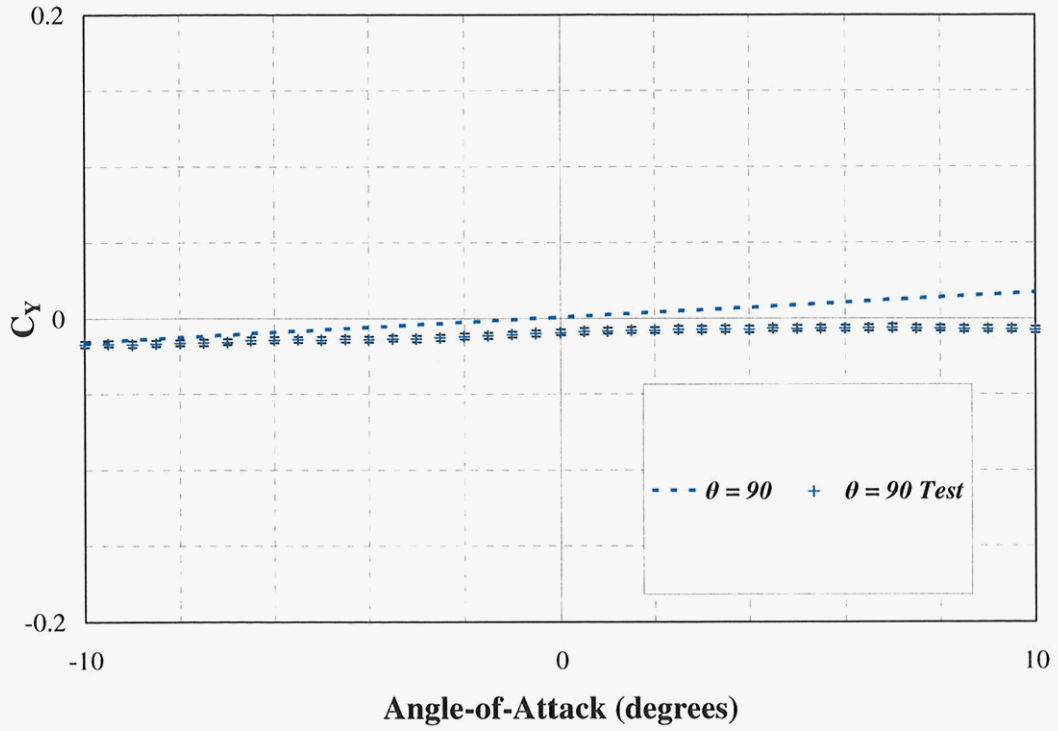
*Figure 35. Side Force Comparison for AR = 1.8824 at Mach 3.0*
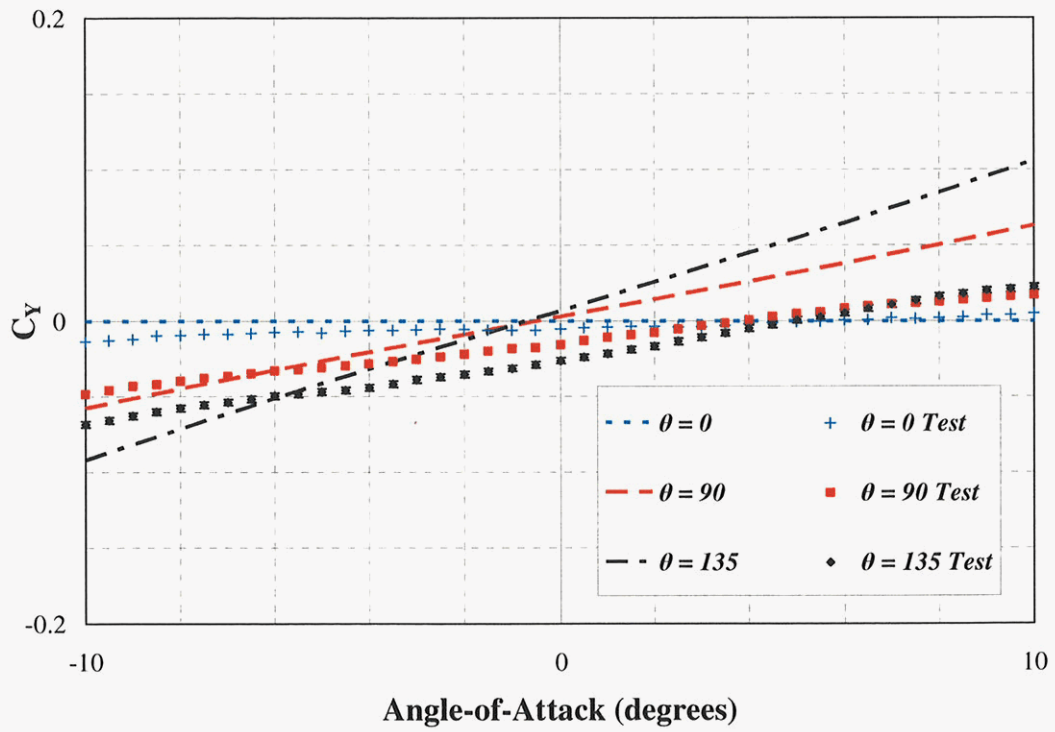
*Figure 36. Side Force Comparison for AR = 2.8333 at Mach 1.5*

30
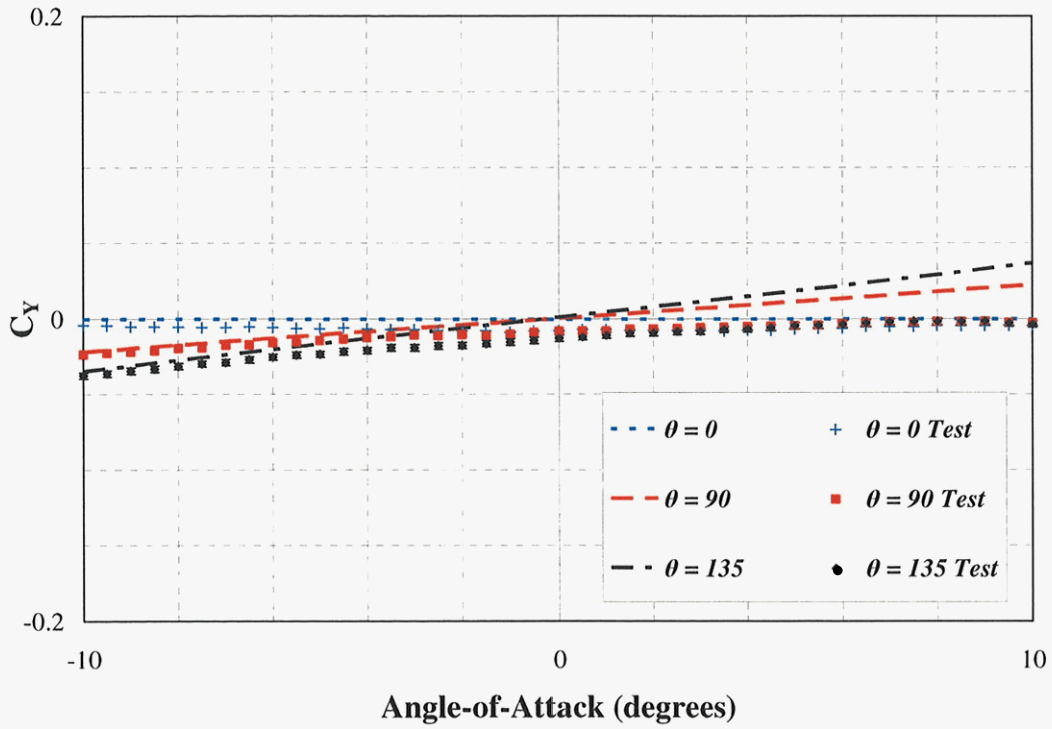
*Figure 37. Side Force Comparison for AR = 2.8333 at Mach 2.25*
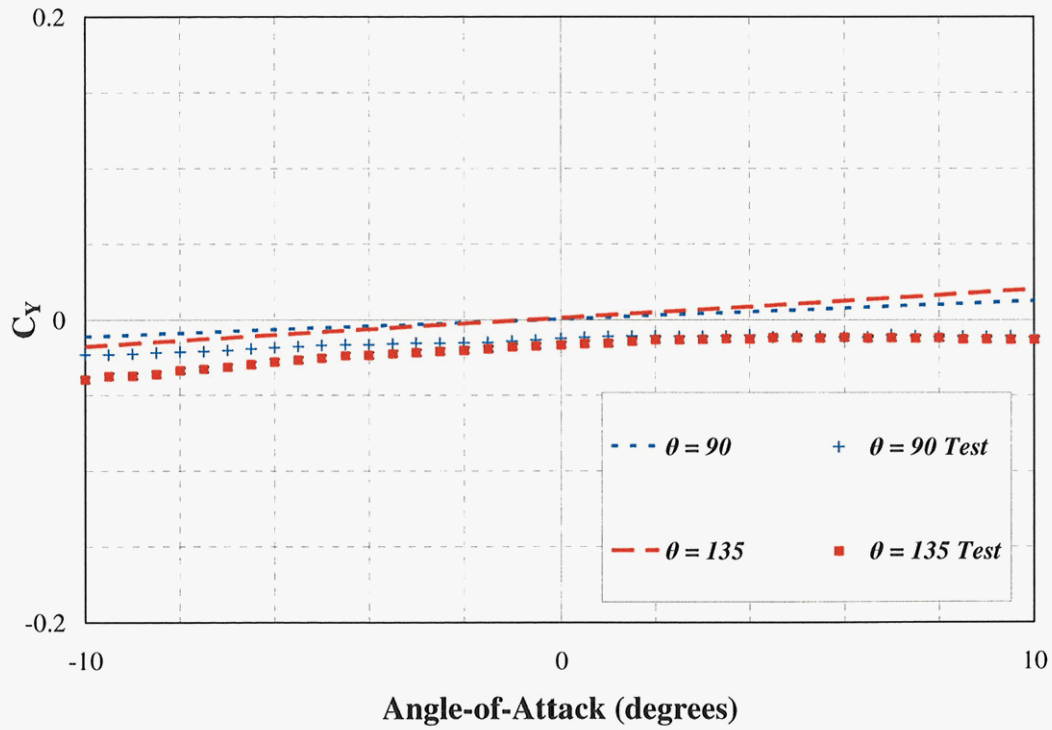
*Figure 38. Side Force Comparison for AR = 2.8333 at Mach 3.0*

31
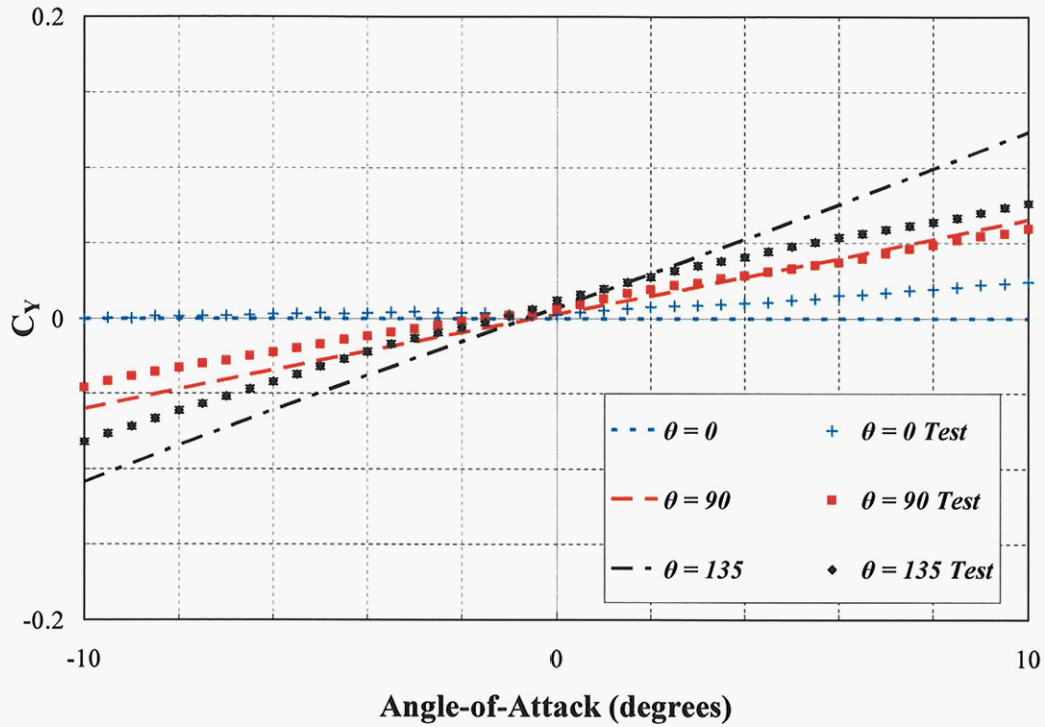
Figure 39. Side Force for AR = 1.8824; Λ = 35° at Mach 1.5

3.   Root Bending Moment

The span-wise CP of the fins is modeled well with the theory as reflected in the root bending moment comparisons seen in Figures 40 through 49. The root bending moment is a combination of the normal and side forces with their respective moment arms (Equation (37)). While the root bending moment is modeled accurately at low incidence, the theory tends to under-predict the root bending moment at higher AoA. The root thickness is most likely moving the span-wise CP of the tested fins towards the fin tip, thus increasing the root bending moment. At negative AoA, the root bending moment is less sensitive to fin curvature.
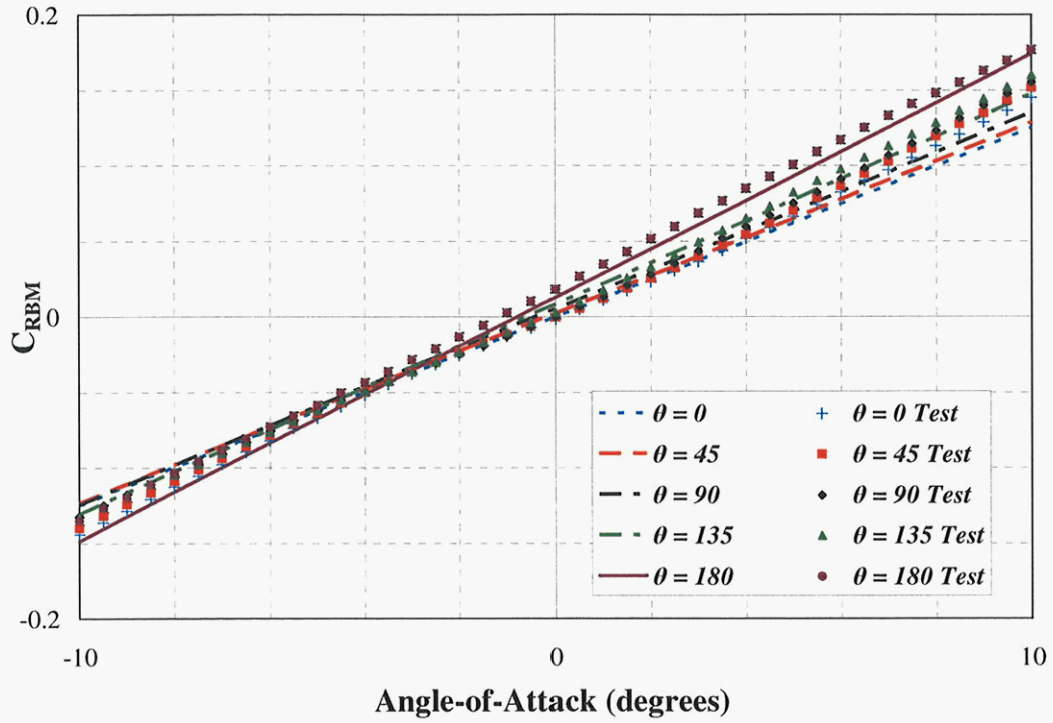
*Figure 40. Root Bending Moment Comparison for AR = 1.4118 at Mach 1.5*
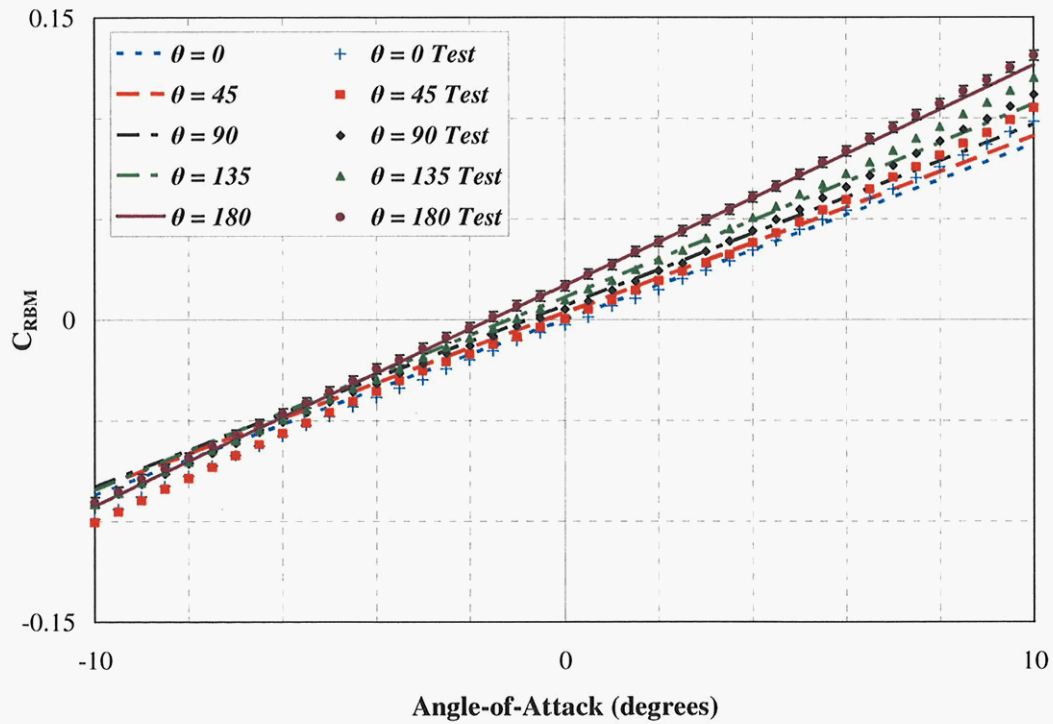
*Figure 41. Root Bending Moment Comparison for AR = 1.4118 at Mach 2.25*
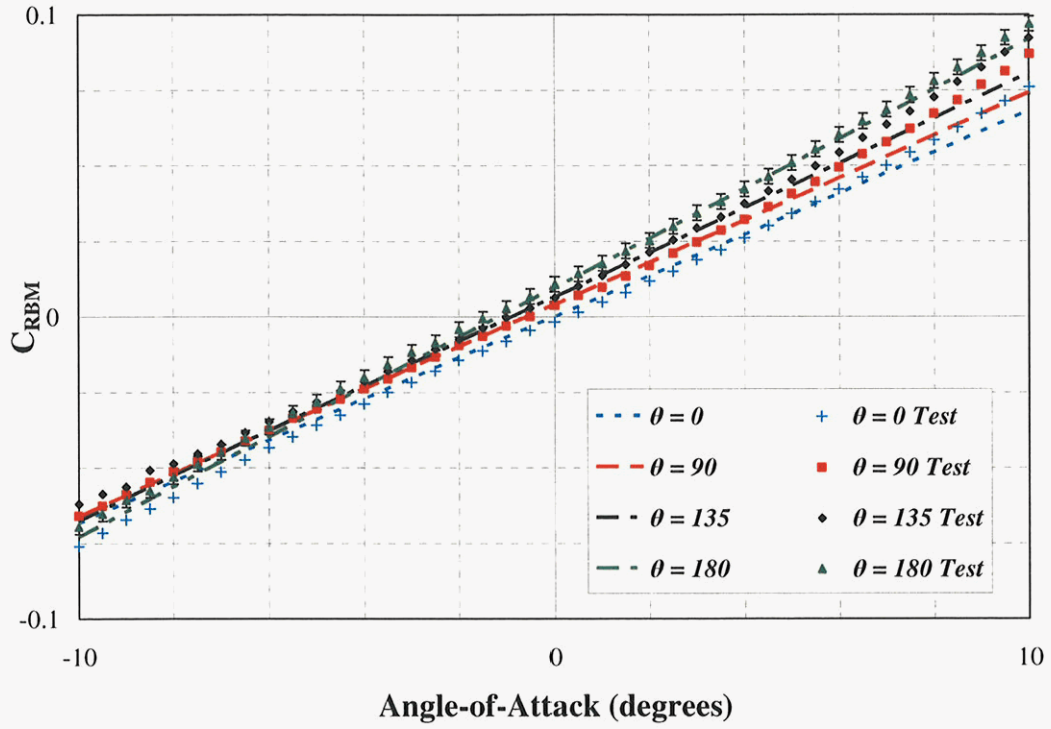
Figure 42. Root Bending Moment Comparison for AR = 1.4118 at Mach 3.0
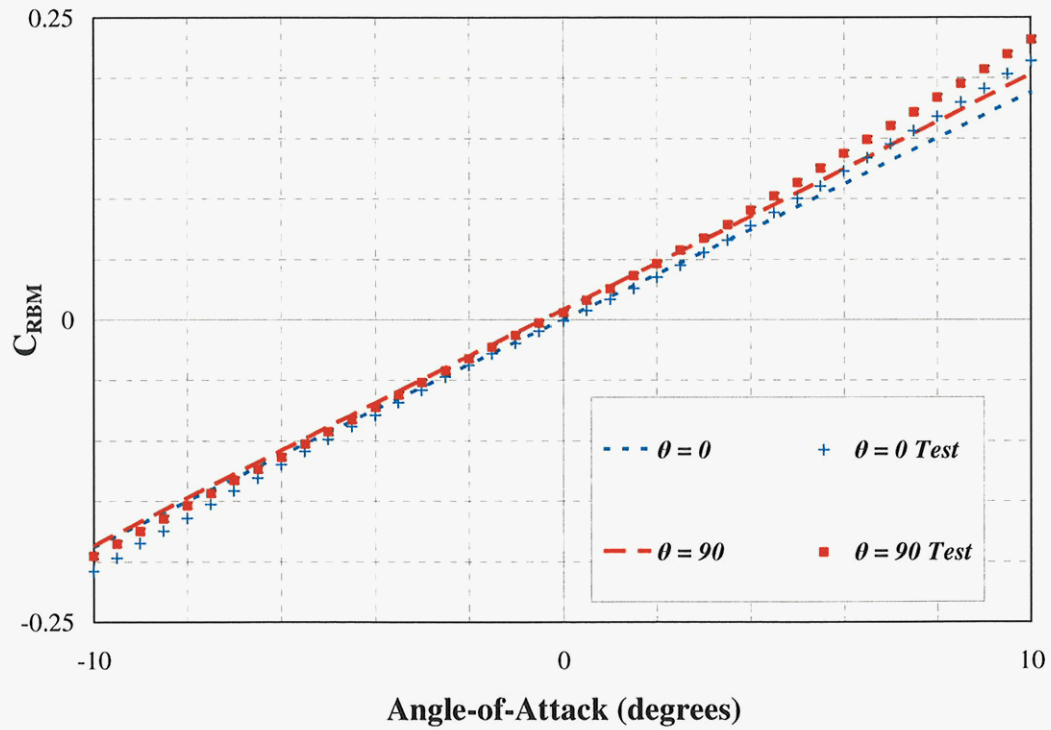

Figure 43. Root Bending Moment Comparison for AR = 1.8824 at Mach 1.5
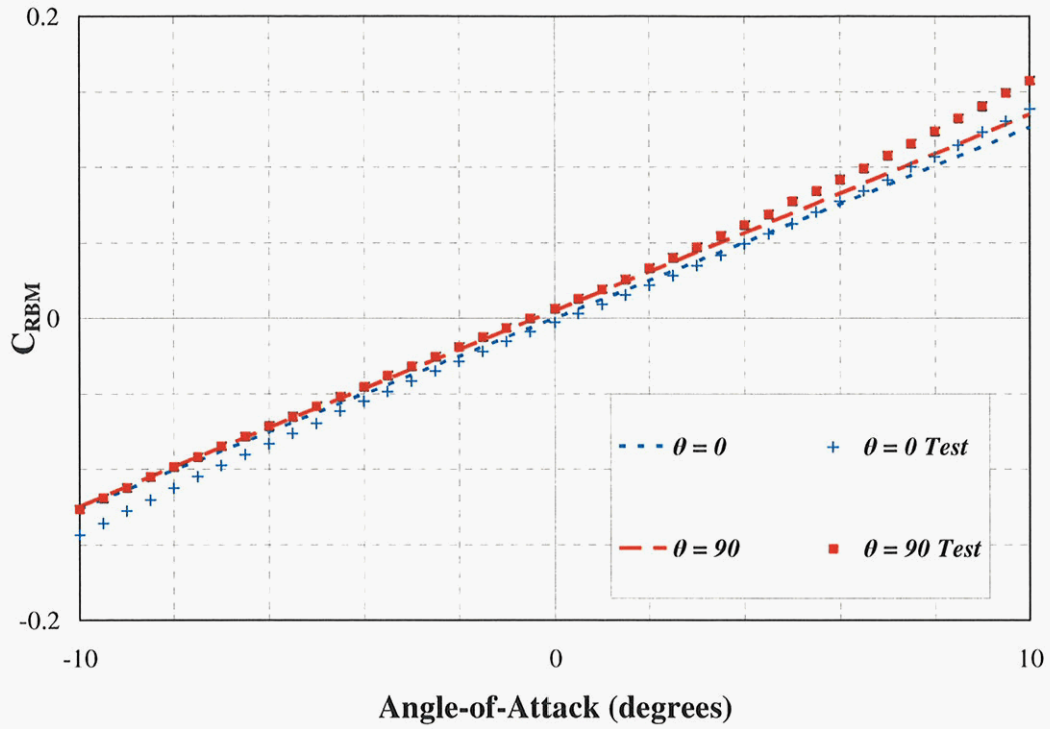
Figure 44. Root Bending Moment Comparison for AR = 1.8824 at Mach 2.25
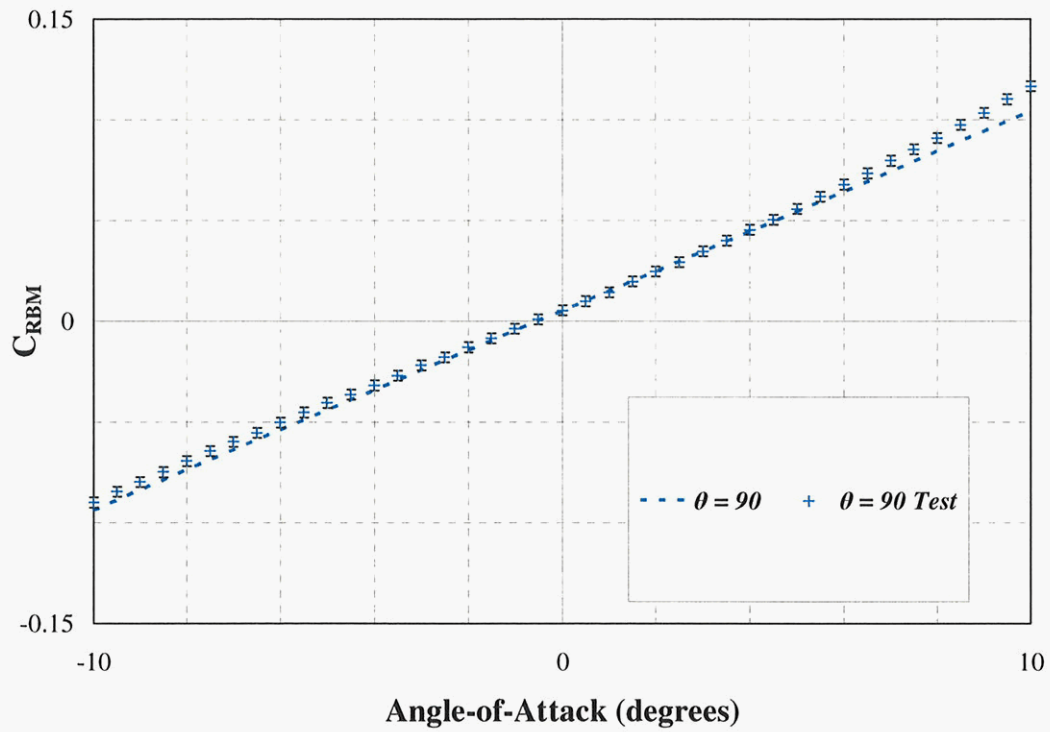
Figure 45. Root Bending Moment Comparison for AR = 1.8824 at Mach 3.0
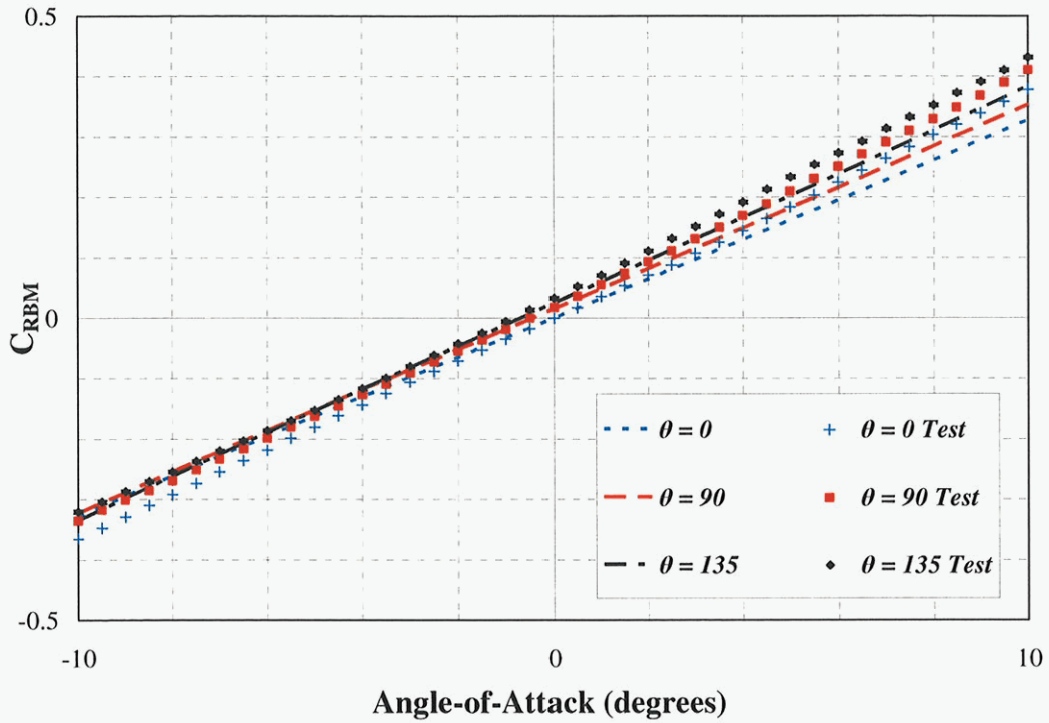
Figure 46. Root Bending Moment Comparison for AR = 2.8333 at Mach 1.5
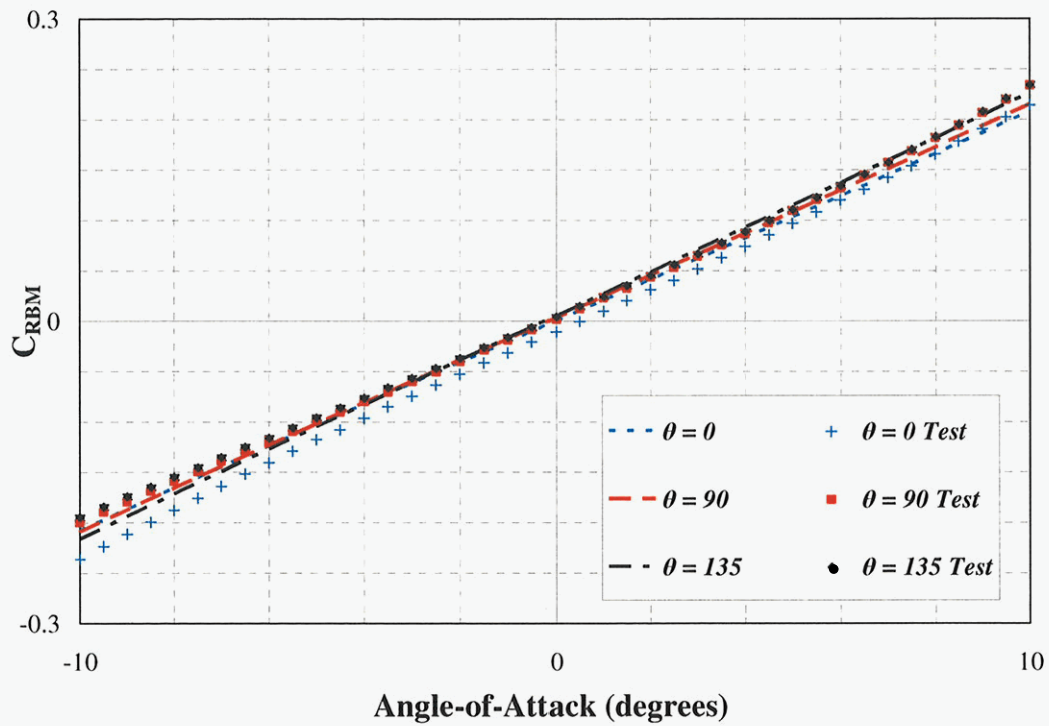

*Figure 47. Root Bending Moment Comparison for AR = 2.8333 at Mach 2.25*
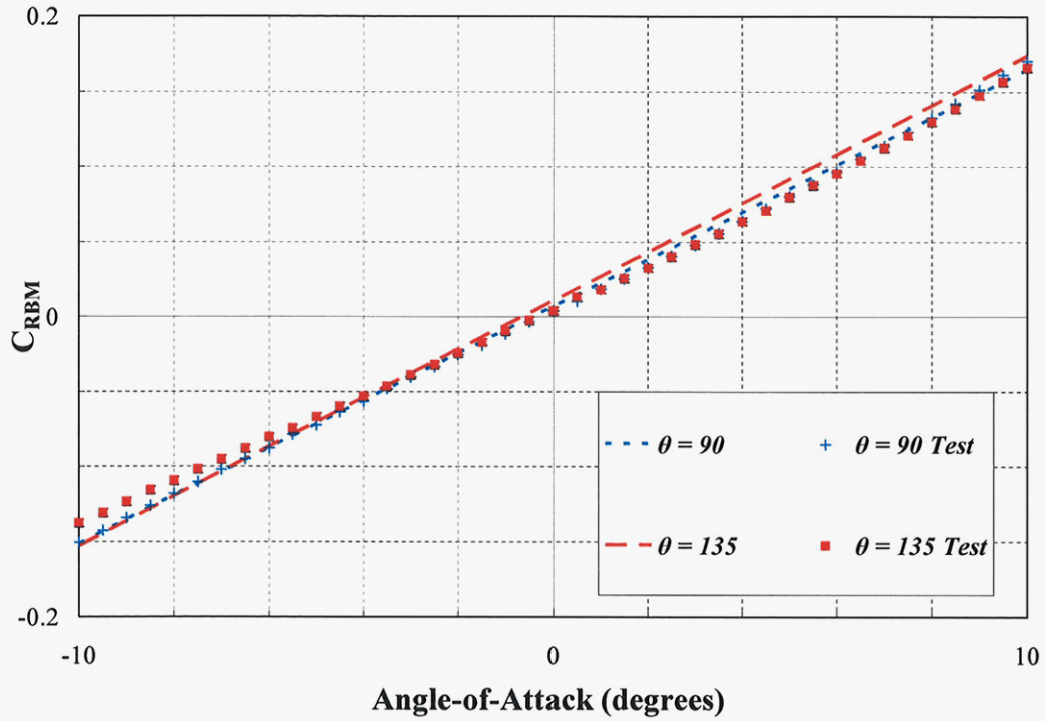
*Figure 48. Root Bending Moment Comparison for AR = 2.8333 at Mach 3.0*
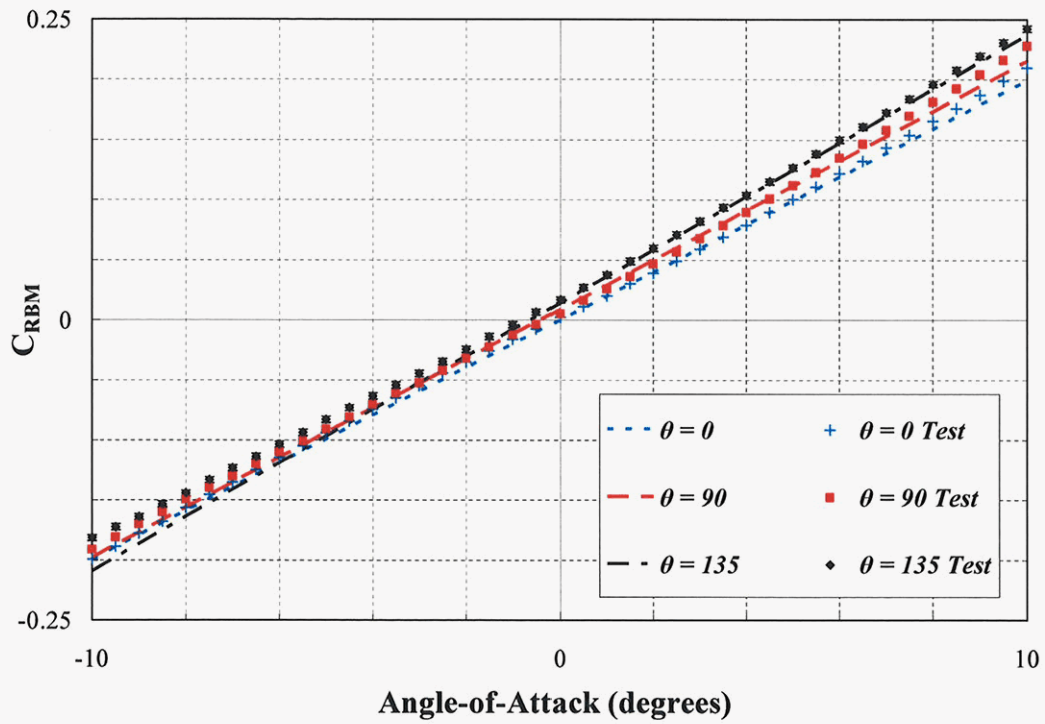
Figure 49. Root Bending Moment for AR = 1.8824; Λ = 35° at Mach 1.5

4. Hinge Moment

The hinge moment data are presented in Figures 50 through 59 about the mid-root chord since fins are typically hinged about their theoretical Center-of-Pressure (CP). As a result, the hinge moments are very small, and the differences between theoretical and test results are visually amplified. Presenting the data about the mid-root chord gives a better indication of the chord-wise CP accuracy. The test results indicate that the CP is more forward than the theoretical results. Since the test articles were not infinitely thin, a shock wave from the leading edge is suspected to decrease the Mach number over the fin, which would shift the CP forward. As seen in Table 4, the chord-wise CP of the fin is modeled within 5- to 10-percent relative error of the test results. As a result of matching both the normal force coefficient and the chord-wise CP reasonably well, the hinge moment comparison yields reasonable results.

Table 4. Chord-Wise CP Non-Dimensionalized by L_{REF}

| AR	θ	Wind-Tunnel Mach 1.5	Theory Mach 1.5	Percent Difference	Wind-Tunnel Mach 2.25	Theory Mach 2.25	Percent Difference	Wind-Tunnel Mach 3.0	Theory Mach 3.0	Percent Difference
1.4118	0	0.3833	0.4265	10.12%	0.4398	0.4663	5.69%	0.4383	0.4786	8.41%
1.4118	45	0.3845	0.4264	9.81%	0.4413	0.4663	5.37%	**	0.4786	**
1.4118	90	0.3951	0.4257	7.18%	0.4383	0.4664	6.04%	0.4425	0.4791	7.66%
1.4118	135	0.3892	0.4241	8.21%	0.4428	0.4674	5.25%	0.4638	0.4812	3.60%
1.4118	180	0.3914	0.4215	7.13%	0.4487	0.4724	5.02%	0.4655	0.4869	4.40%
1.8824	0	0.4081	0.4487	9.04%	0.4408	0.4770	7.59%	**	0.4854	**
1.8824	90	0.4122	0.4482	8.03%	0.4589	0.4775	3.90%	0.4496	0.4862	7.53%
2.8333	0	0.4207	0.4706	10.59%	0.4391	0.4867	9.79%	**	0.4918	**
2.8333	90	0.4158	0.4708	11.68%	0.4409	0.4875	9.56%	0.4200	0.4926	14.75%
2.8333	135	0.4309	0.4722	8.76%	0.4610	0.4897	5.88%	0.4675	0.4946	5.49%
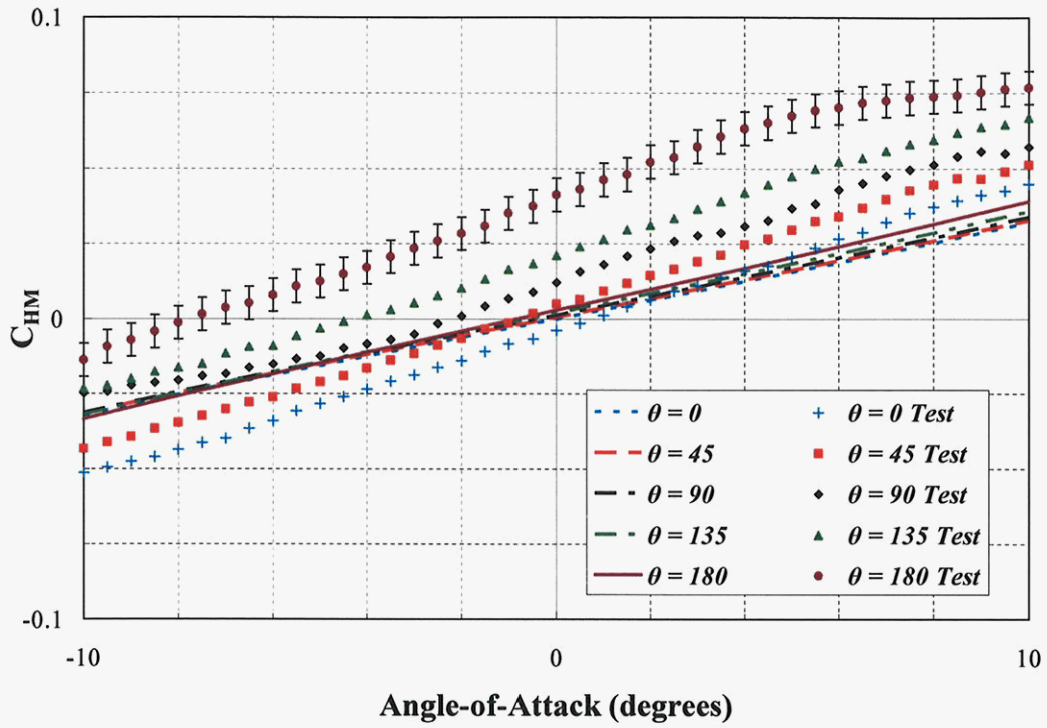
Figure 50. Hinge Moment About $C_R/2.0$ Comparison for AR = 1.4118 at Mach 1.5
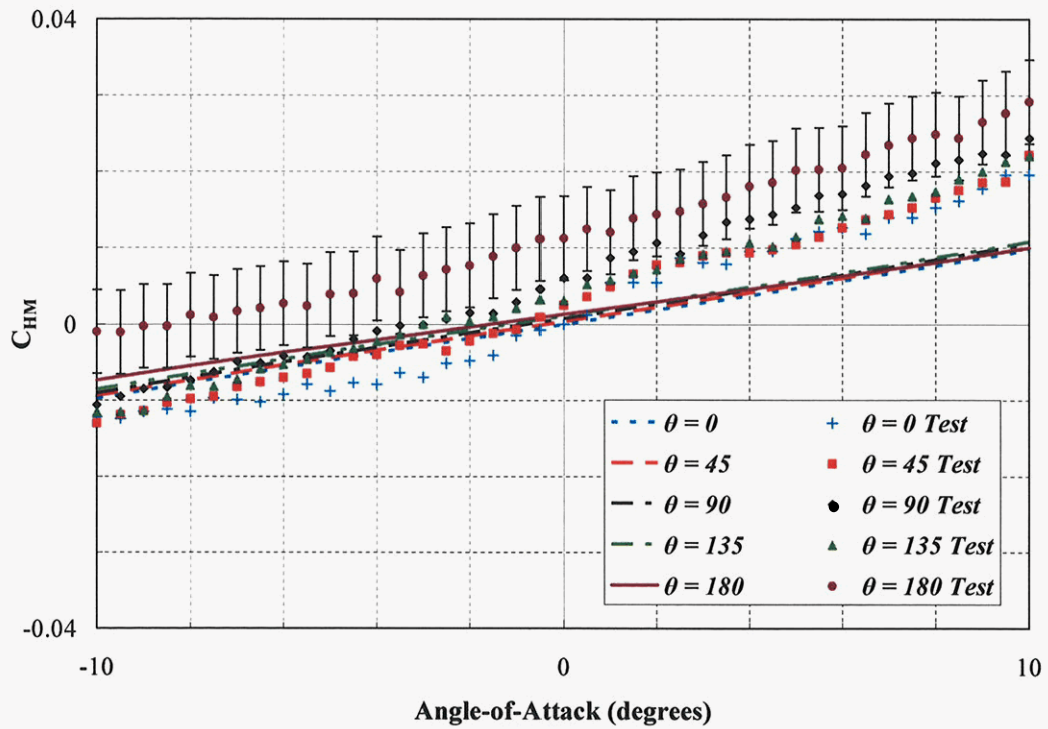
Figure 51. Hinge Moment About $C_R/2.0$ Comparison for AR = 1.4118 at Mach 2.25
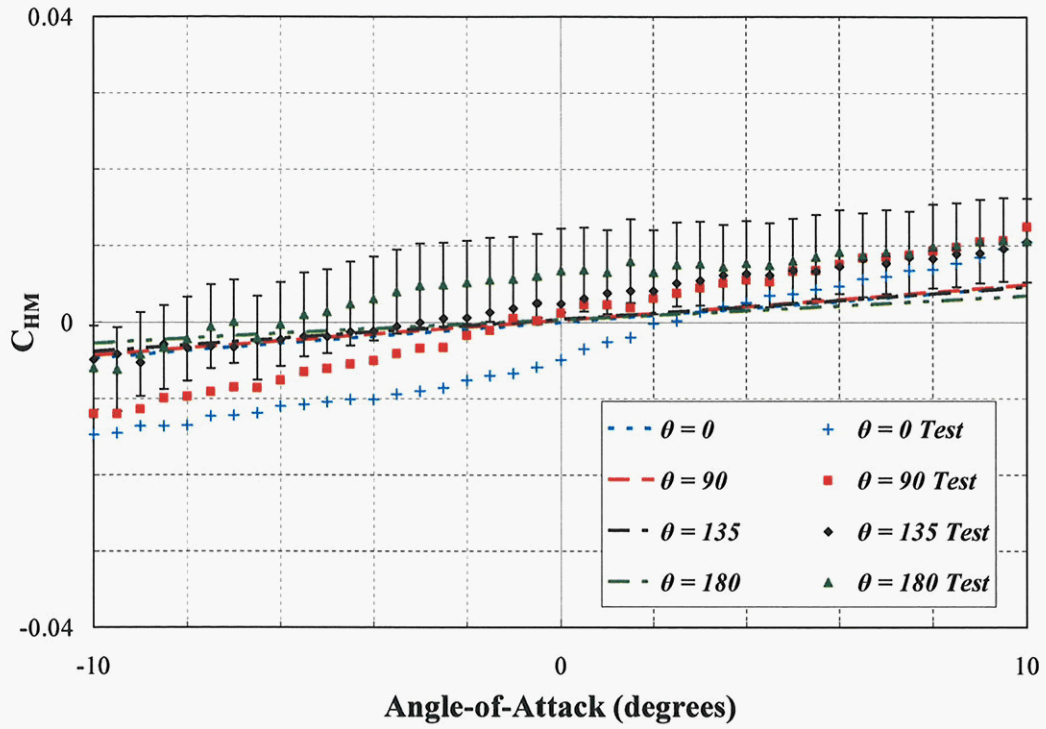
Figure 52. Hinge Moment About $C_R/2.0$ Comparison for AR = 1.4118 at Mach 3.0
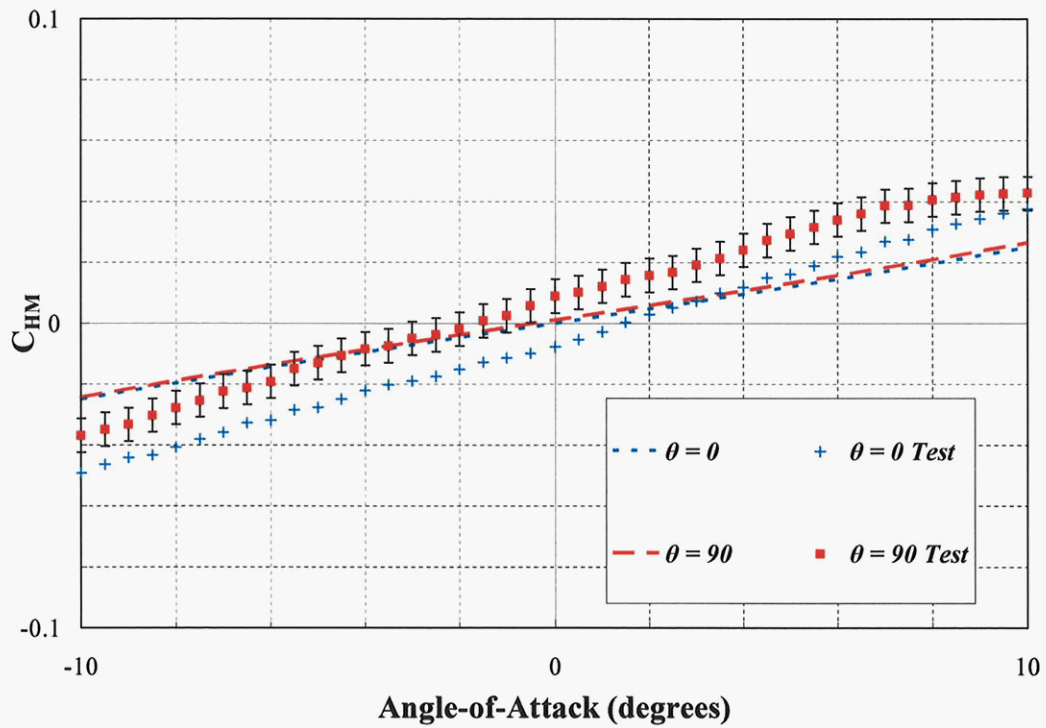
Figure 53. Hinge Moment About $C_R/2.0$ Comparison for AR = 1.8824 at Mach 1.5
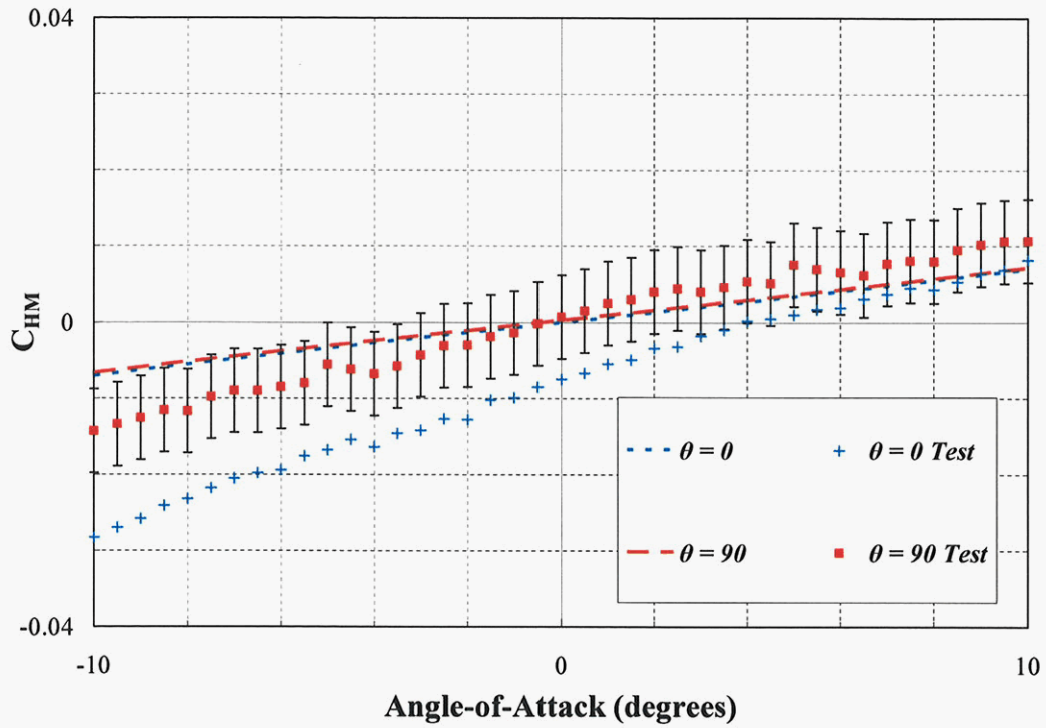
Figure 54. Hinge Moment About $C_R/2.0$ Comparison for AR = 1.8824 at Mach 2.25
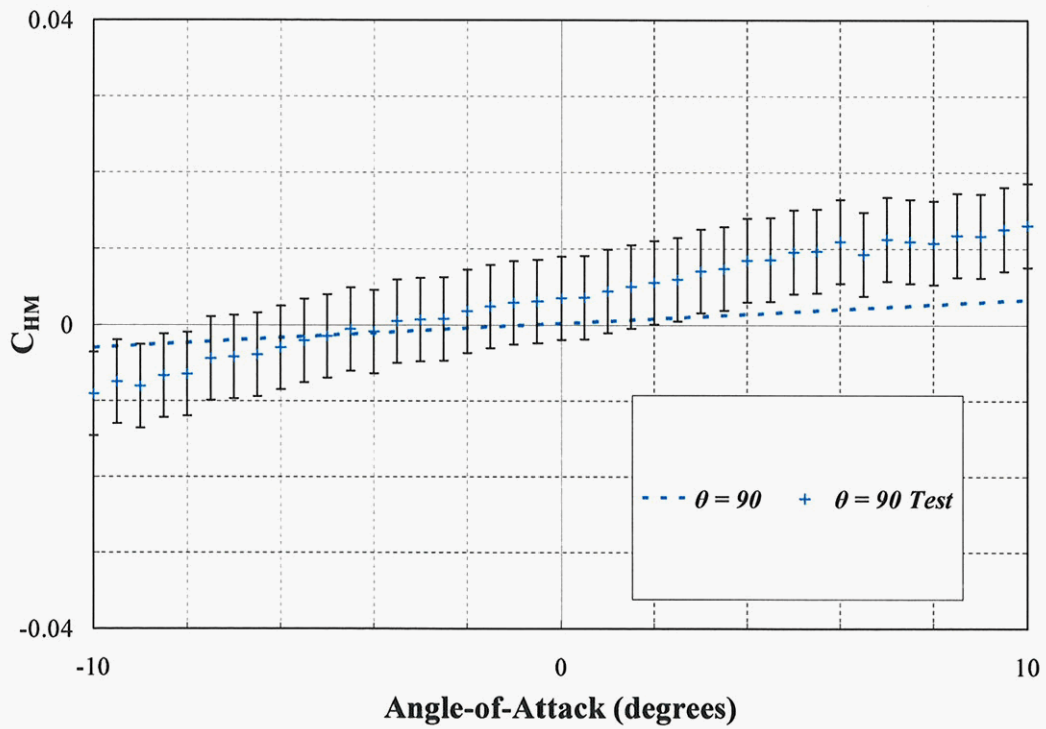
Figure 55. Hinge Moment About $C_R/2.0$ Comparison for AR = 1.8824 at Mach 3.0
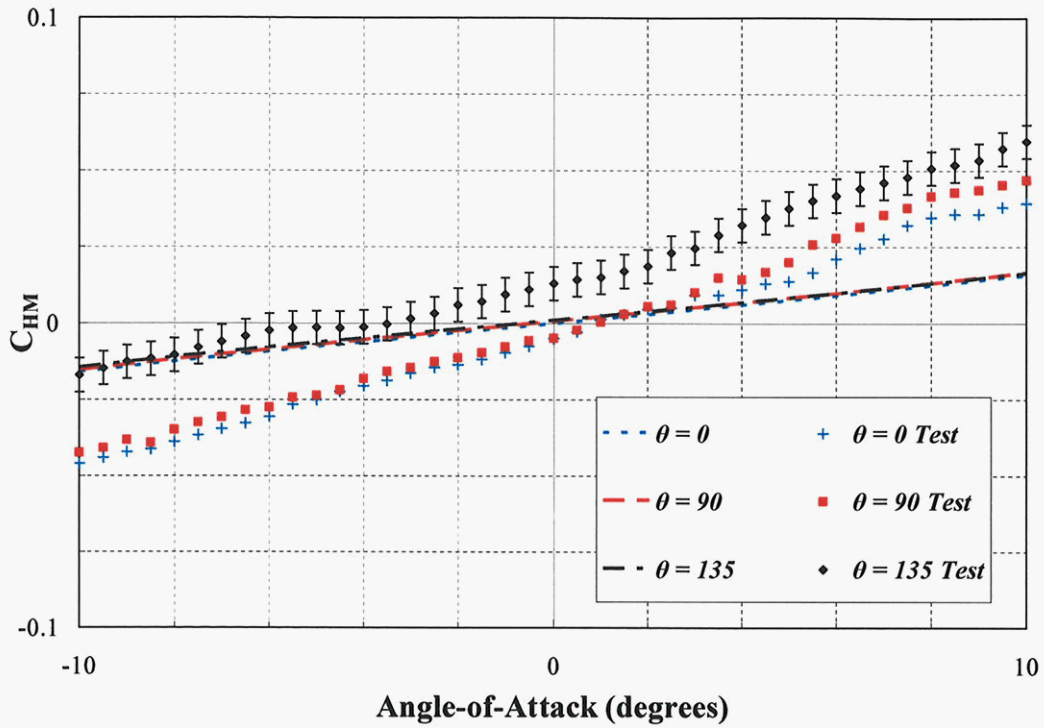
Figure 56. Hinge Moment About $C_R/2.0$ Comparison for AR = 2.8333 at Mach 1.5
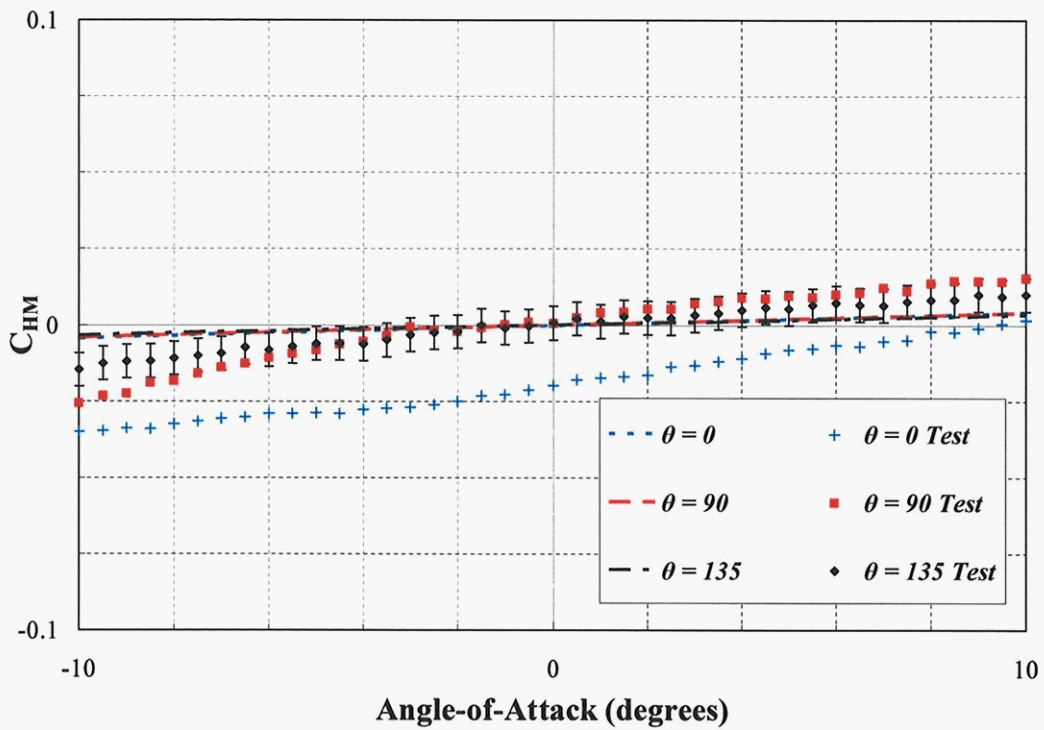
*Figure 57. Hinge Moment About $C_R/2.0$ Comparison for AR = 2.8333 at Mach 2.25*
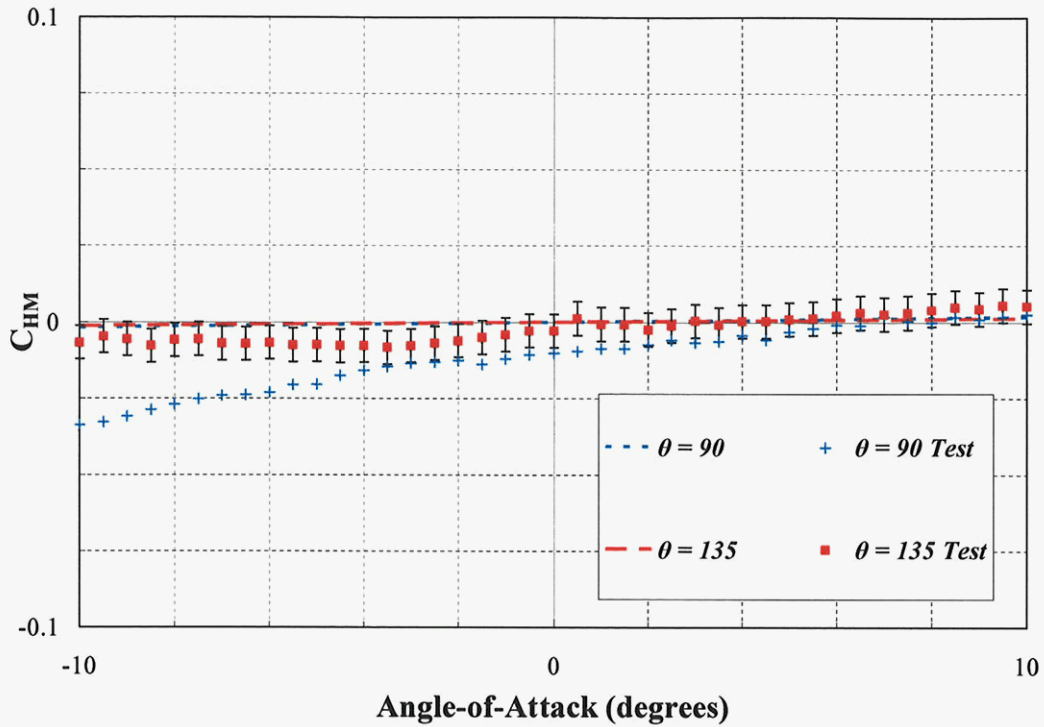
*Figure 58. Hinge Moment About CR/2.0 Comparison for AR = 2.8333 at Mach 3.0*
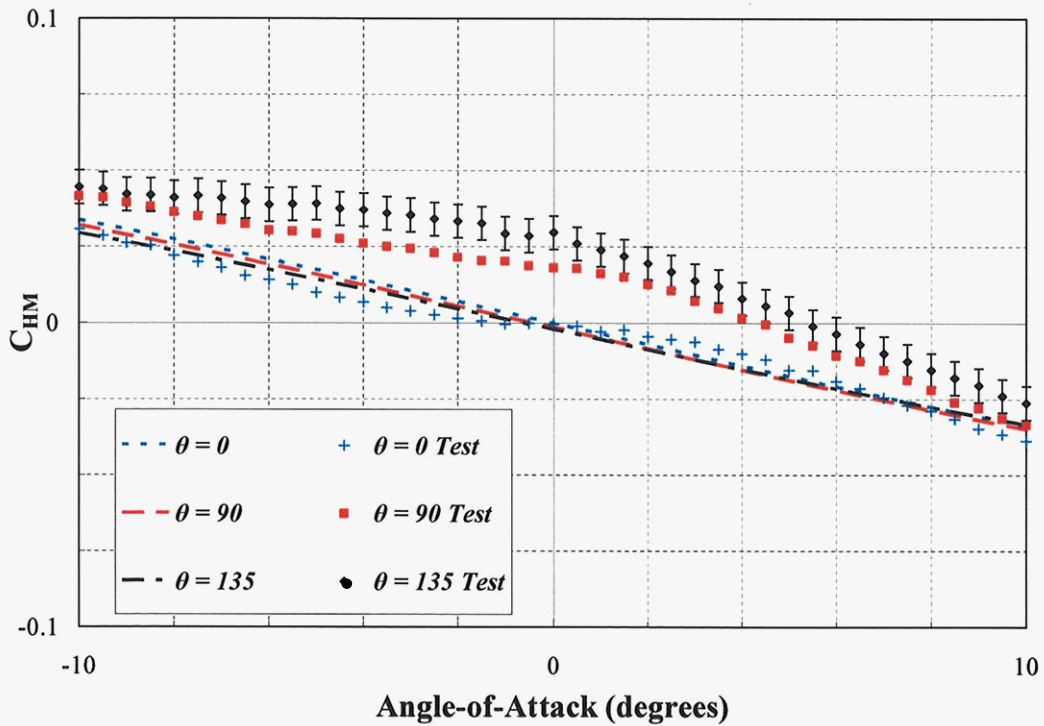
Figure 59. Hinge Moment About C_R/2.0 for AR = 1.8824; Λ = 35° at Mach 1.5

B. Pressure Contour Plots

Pressure contour plots are presented in Figures 60 through 71 for 5 degrees AoA to show the effects of fin curvature and Mach number. The pressure contour plots can give another dimension to the aerodynamic assessment of WAFs. The CPs can be visualized and areas of high-pressure differential can be identified for possible fin redesign. The figures are arranged to show the effects of Mach number on each row and the effects of fin curvature on each column.

The CP moves aft and toward the fin tip as the Mach number increases. The area of higher pressure differential (Region I) enlarges with increasing fin curvature. Potential performance enhancements could be generated based on analysis of the pressure contour plots such as clipping the trailing edge fin tip to decrease the fin surface area, while retaining the fin region which produces a majority of the stabilizing force.

Fin curvature also increases the area of the fin in the xz-plane, which creates a higher side force. Since fins are typically used in sets, the net fin side forces are cancelled; however, the side force can generate a rolling moment when the CP is located at a non-zero z-coordinate. While the induced fin normal force generates a majority of the induced rolling moment on a missile equipped with WAFs, the fin side force contributions must be known to accurately model the overall missile rolling moment.
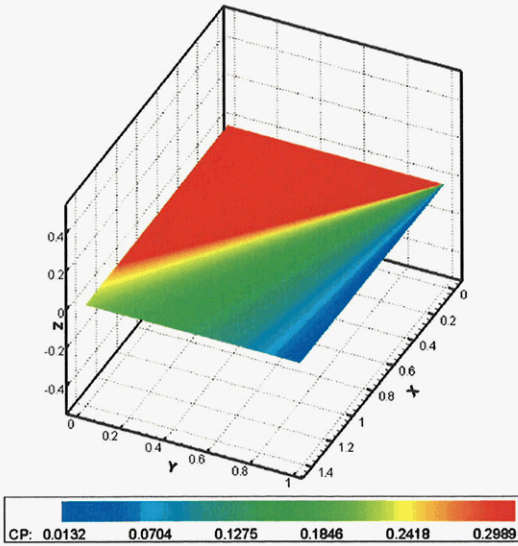
Figure 60. Pressure Contour for θ = 0.0;
AR = 1.4118 at Mach 1.5
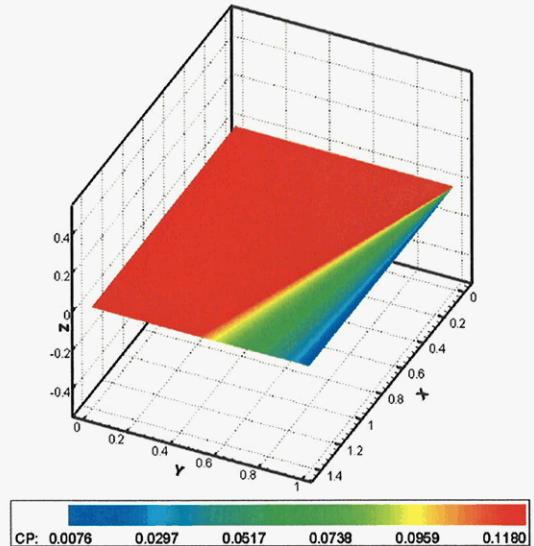
Figure 61. Pressure Contour for
θ = 0.0; AR = 1.4118 at Mach 3.0
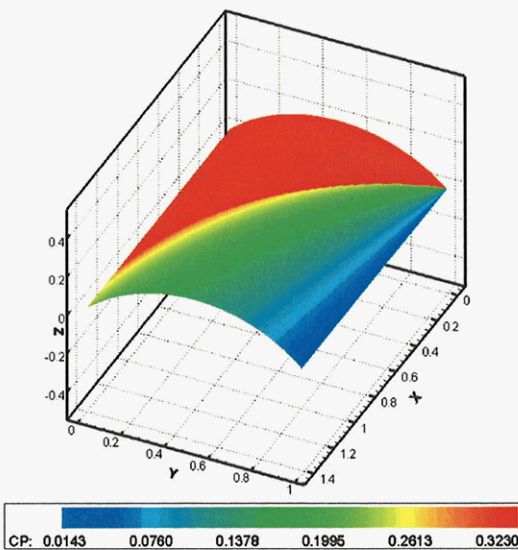
Figure 62. Pressure Contour for θ = 90.0;
AR = 1.4118 at Mach 1.5
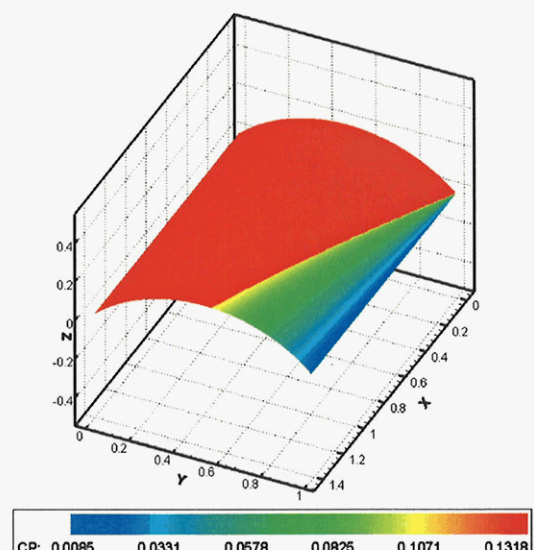
Figure 63. Pressure Contour for
θ = 90.0; AR = 1.4118 at Mach 3.0
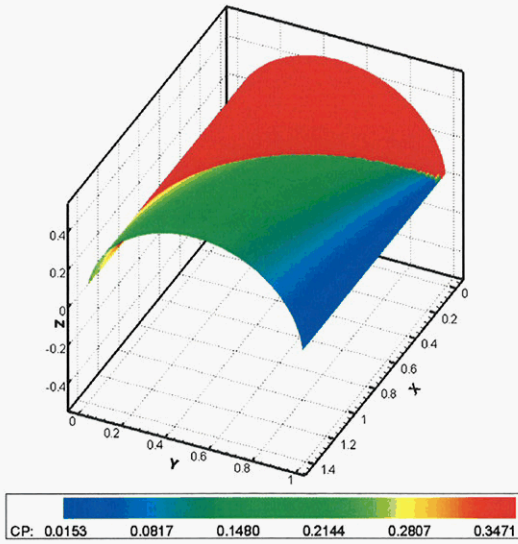
Figure 64. Pressure Contour for θ = 180.0;
AR = 1.4118 at Mach 1.5
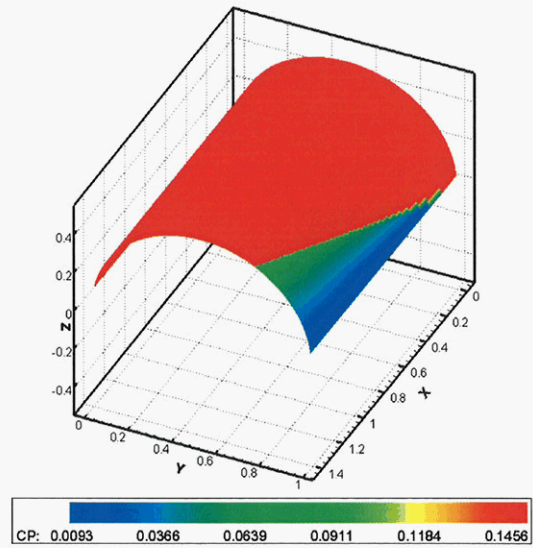
Figure 65. Pressure Contour for
θ = 180.0; AR = 1.4118 at Mach 3.0
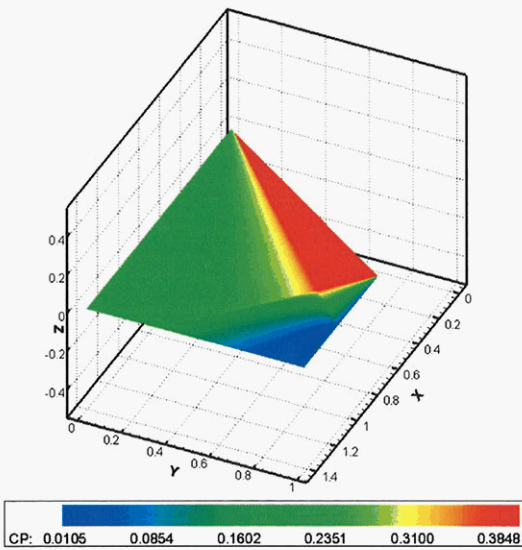
Figure 66. Pressure Contour for Λ = 35.0;
θ = 0.0; AR = 1.8824 at Mach 1.5
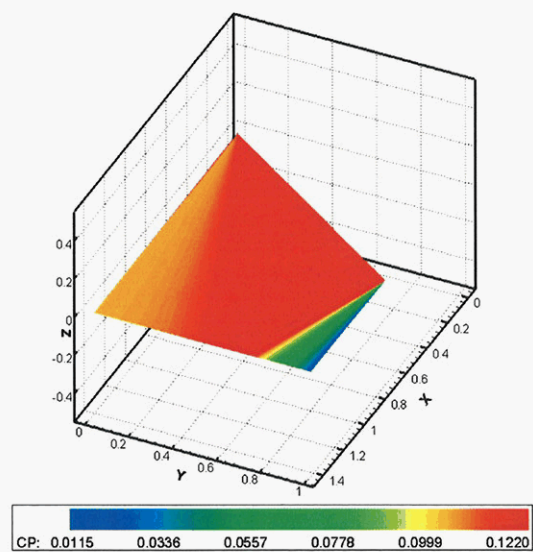
Figure 67. Pressure Contour for
Λ = 35.0; θ = 0.0; AR = 1.8824 at
Mach 3.0

46
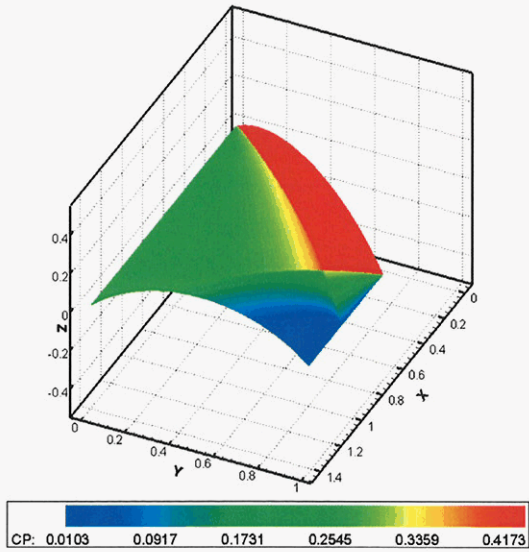
Figure 68. Pressure Contour for Λ = 35.0;
θ = 90.0; AR = 1.8824 at Mach 1.5
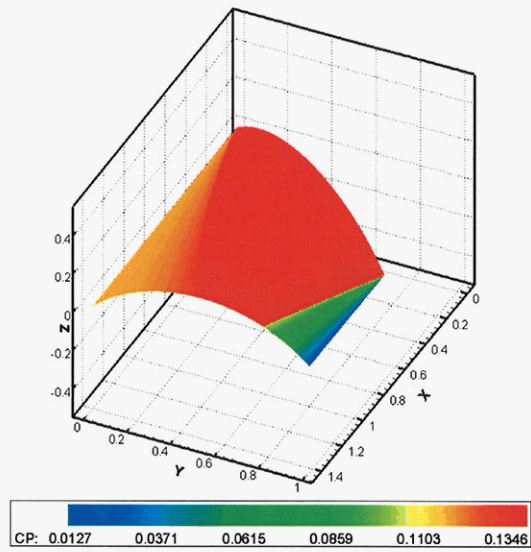
Figure 69. Pressure Contour for
Λ= 35.0; θ = 90.0; AR = 1.8824 at
Mach 3.0
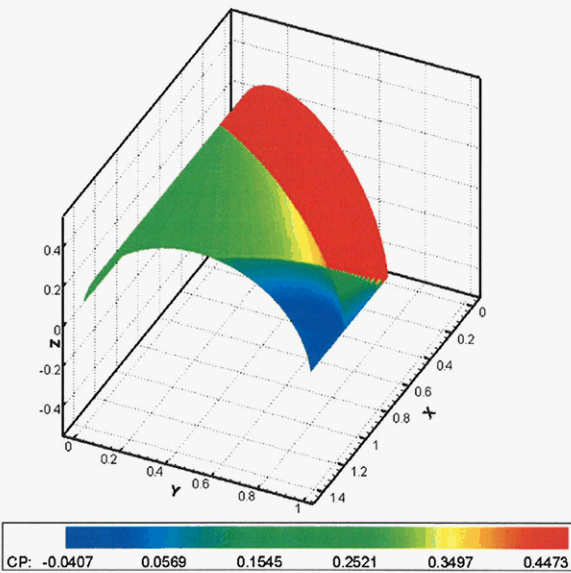
Figure 70. Pressure Contour for Λ = 35.0;
θ = 180.0; AR = 1.8824 at Mach 1.5
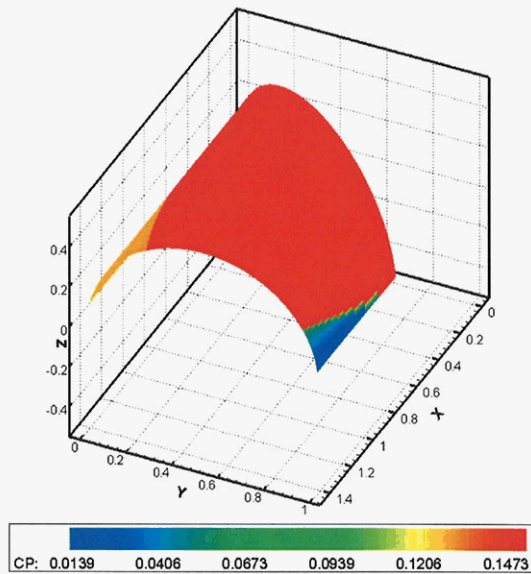
Figure 71. Pressure Contour for
Λ = 35.0; θ = 180.0; AR = 1.8824 at
Mach 3.0

47

VI. LIMITATIONS

While several fin parameters and flow conditions were used to present a generalized method of estimating the pressure-driven forces and moments of a WAF, the methodology has Mach number, aspect ratio, leading edge sweep angle, and thickness-to-chord ratio limits based on the tested fin parameters. The empirical fit for induced AoA is based on data collected on rectangular fins from Mach 1.5 to Mach 3.0, with aspect ratios ranging from 1.4118 to 2.8333. The thickness-to-chord ratio for all the fins varied linearly from 3 percent at the root to 1.5 percent at the tip (with the exception of the thickened root). The method compares well to wind-tunnel results for these fins; however, no proof exists that this correlation applies to fins with features outside the test envelope. The methodology to compute the pressure differential is derived from potential flow theory for an infinitely thin fin; therefore, the results from the method will represent a thin fin with no boundary layer or shock waves that will never stall. With these limitations stated, the method will provide a reasonable design envelop for typical WAF applications in supersonic flow.

VII. CONCLUSION

A new method has been developed to obtain the pressure loading of curved or WAFs with modifications to existing supersonic fin theory and the aid of recent wind-tunnel test data. The theoretical results show agreement to wind-tunnel test data for the low-incidence forces and moments that have puzzled aerodynamicist for years. The method provides an expedient analysis tool that has been developed to cover a broad range of fin parameters that can be used for roll tailoring or roll minimization on missile systems requiring the use of WAFs.

REFERENCES

1. Abate, G., "Aerodynamic Research of Wraparound Fin Missile Configurations and Alternative Wraparound Fin Designs," WL-TR-94-7015, Wright Laboratory Armament Directorate, Eglin Air Force Base, Florida, February 1994.

2. Ailor, W. H., III, "Supersonic Aerodynamic Characteristics of a Wraparound Folding Fin," IHTR 337, Naval Ordnance Station, Indian Head, Maryland, June 1971.

3. Auman, L. M., "The Aerodynamic Characteristics of Production MLRS Wraparound Fins," Technical Report RD-SS-92-10, U.S. Army Missile Command, Redstone Arsenal, Alabama, August 1992.

4. Auman, L. M., "Aerodynamic Characteristics of a Guided MLRS Rocket," Technical Report RD-SS-98-4, U.S. Army Aviation and Missile Command, Redstone Arsenal, Alabama, December 1997.

5. Butler, R. W., "Evaluation of the Pressure Distribution on the Fins of a Wraparound Fin Model at Subsonic and Transonic Mach Numbers," AEDC-TR-71-273, Air Force Systems Command, Arnold Air Force Station, Tennessee, December 1971.

6. Dahlke, C. W., "Aerodynamics of Wraparound Fins: A Survey of the Literature," RD-TR-71-1, U.S. Army Missile Command, Redstone Arsenal, Alabama, March 1971.

7. Dahlke, C. W. and L. D. Flowers, "The Aerodynamic Characteristics of Wraparound Fins, Including Fold Angle, at Mach Numbers from 0.5 to 1.3," Report No. RD-TR-75-19, U.S. Army Missile Command, Redstone Arsenal, Alabama, December 1974.

8. Dahlke, C. W., "The Aerodynamic Characteristics of Wraparound fins at Mach Numbers of 0.3 to 3.0," Technical Report RD-77-4, U.S. Army Missile Command, Redstone Arsenal, Alabama, October 1976.

9. Dahlke, C. W., R. A. Deep, and V. Oskay, "Techniques for Roll Tailoring for Missiles with Wraparound Fins," AIAA-83-0463, American Institute of Aeronautics and Astronautics 21st Aerospace Science Meeting, Reno, Nevada, January 1983.

10. Dahlke, C. W. and L. D. Flowers, "The Aerodynamic Characteristics of Wraparound Fins, Including Fold Angle, at Mach Numbers from 0.5 to 1.3," Technical Report RD-75-19, U.S. Army Missile Command, Redstone Arsenal, Alabama, December 1974.

11. Evvard, J. C., "Distribution of Wave Drag and Lift in the Vicinity of Wing Tips at Supersonic Speeds," NACA Technical Note No. 1382, Flight Propulsion Research Laboratory, Cleveland, Ohio, July 1947.

REFERENCES (CONCLD)

12. Evvard, J. C., "Theoretical Distribution of Lift on Thin Wings at Supersonic Speeds," NACA Technical Note No. 1585, Flight Propulsion Research Laboratory, Cleveland, Ohio, May 1948.

13. Harmon, S. M. and Isabella Jeffreys, "Theoretical Lift and Damping in Roll of Thin Wings with Arbitrary Sweep and Taper at Supersonic Speeds," NACA Technical Note No. 2114, Langley Aeronautical Laboratory, Langley Air Force Base, Virginia, May 1950.

14. McIntyre, T. C., R. D. W. Bowersox, and L. P. Goss, "Effects of Mach Number on Supersonic Wraparound Fin Aerodynamics," Journal of Spacecraft and Rockets, Vol. 35, No. 6, November-December 1998.

15. Mirels, Harold, "Theoretical Wave Drag and Lift of Thin Supersonic Ring Airfoils," NACA Technical Note No. 1678, Flight Propulsion Laboratory, Cleveland, Ohio, August 1948.

16. Moeckel, W. E. and J. C. Evvard, "Load Distribution due to Steady Roll and Pitch for Thin Wings at Supersonic Speeds," NACA Technical Note No. 1689, Flight Propulsion Research Laboratory, Cleveland, Ohio, August 1948.

17. Robinson, M. L. and C. E. Fenton, "Static Aerodynamic Characteristics of a Wraparound Fin Configuration with Small Rolling Moments at Low Incidence," WRE-Technical Note-527 (WR&D), Australian Defence Scientific Service, Salisbury, South Australia, November 1971.

18. Tilmann, C. P., R. E. Huffman, Jr., T. A. Bulter, and R. D. W. Bowersox, "Characterization of the Flow Structure in the Vicinity of a Wraparound Fin at Supersonic Speeds," American Institute of Aeronautics and Astronautics 34th Aerospace Science Meeting, AIAA 96-0190, Reno, Nevada, January 1996.

LIST OF ACRONYMS AND SYMBOLS

AoA	Angle-of-Attack
AMRDEC	Army Missile Research, Development and Engineering Center
APKWS	Advanced Precision Kill Weapon System
BAT	Brilliant Anti-armor Technology
CAD	Computer-Aided Drafting
CFD	Computational Fluid Dynamics
CP	Center-of-Pressure
CKEM	Compact Kinetic Energy Missile
HSWT	High Speed Wind-Tunnel
LMMFC	Lockheed Martin Missile and Fire Control
LOSAT	Line-of-Sight Antitank
MLRS	Multiple Launch Rocket System
TACAWS	The Army Combined Arms Weapons System
USAF	United States Air Force
WAF(s)	Wraparound Fin(s)
C_N	Normal Force Coefficient
C_{RBM}	Root Bending Moment Coefficient
C_Y	Side Force Coefficient
C_{HM}	Hinge Moment Coefficient
$\Delta A_{x,y}$	Incremental Fin Panel Surface Area Projected onto xy-Plane
Δx	Incremental Chord-wise Length
Δy	Incremental Span-wise Length
Δz	Incremental Curve-wise Length
b	Wingspan
b/2	Fin semi-span
L_{REF}	Mean Chord Length
S_{REF}	Fin Plan-form Area, L_{REF} (b/2)
AR	Fin Aspect Ratio, $b^2/(2.0\ S_{REF})$
α	Angle-of-Attack
$\alpha_{INDUCED}$	Induced Angle-of-Attack
$\alpha_{AERODYNAMIC}$	Angle Between the Free-stream Mach number and the Fin Chord
$M,\ M_\infty$	Free-stream Mach number
b	Compressibility Factor, $\sqrt{M^2 - 1.0}$
δ	Fin Curvature slope angle
Λ	Leading Edge Sweepback Angle
θ	Fin Curvature

INITIAL DISTRIBUTION LIST

Copies

Weapon Systems Technology Information Analysis Center   1
ATTN: Ms. Vakare Valaitis
1901 N. Beauregard Street, Suite 400
Alexandria, VA 22311-1720

Defense Technical Information Center   1
8725 John J. Kingman Rd., Suite 0944
Fort Belvoir, VA 22060-6218

Aeroprediction, Inc.
ATTN: Dr. Frank Moore   1
9449 Grover Drive, Suite 201
King George, VA 22485

Director, DIA, MSIC
ATTN: MSD-2, Mr. Jon Hall   1
Building 4545
Redstone Arsenal, AL 35898-5500

Dynetics, Inc.
ATTN: Mr. Mark Miller   1
ATTN: Mr. Wayne Dahlke   1
1000 Explorer Blvd.
Huntsville, AL 35806

Eglin Air Force Base
ATTN: Greg Abate   1
101 W. Eglin Blvd., Ste. 332
Eglin AFB, FL 32542

Lockheed Martin Missile and Fire Control – EM-55
ATTN: Mr. Harry Barnard   1
P. O. Box 650003
Dallas, TX 75265-0003

NASIC/AENW
ATTN: James Simon   1
4180 WSatson Way
WPAFB, OH 45433

Nielson Engineering & Research, Inc.
ATTN: Dr. Marnix Dillenius   1
526 Clyde Avenue
Mountain View, CA 94043-2212

INITIAL DISTRIBUTION LIST (CONCLD)

<u>Copies</u>

Raytheon Company
ATTN: Mr. David Corder   1
P. O. Box 11337
Bldg. M02, M/S T3
Tucson, AZ 85734-1337

AMSRD-AMR   (Electronic)

AMSRD-AMR-IN-IC   2

AMSRD-AMR-SS,   Mr. Greg Tackett   1

AMSRD-AMR-SS-AT,   Mr. Brett L. Wilks   1
                            Mr. Lamar M. Auman   1

AMSRD-L-G-I,   Mr. Dayn Beam   1